Physics – Uspekhi **65** (7) 677 – 705 (2022) ©2022 Uspekhi Fizicheskikh Nauk, Russian Academy of Sciences

INSTRUMENTS AND METHODS OF INVESTIGATION PACS numbers: 29.25.Ni, **36.40. – c**, **41.75. – i**, 68.49.Sf

Gas-dynamic sources of cluster ions for basic and applied research

A E Ieshkin, A B Tolstoguzov, N G Korobeishchikov, V O Pelenovich, V S Chernysh

DOI: https://doi.org/10.3367/UFNe.2021.06.038994

Contents

Abstract. State of the art in the development and application of gas cluster ion sources is considered. The mechanisms of neutral cluster formation, the techniques applied to study their flows and regularities of ionization and the principles of mass separation of ion beams are discussed. Design features of some cluster ion beam sources intended for various applied and academic studies are considered. Use of such sources for controlled modification of surface topography, ultra-shallow ion implantation, development of analytical techniques, and stimulation of surface chemical reactions is analyzed.

Keywords: clusters, gas cluster ions, ion sources, supersonic flows, ionization, mass separation, sputtering, self-organization, ion implantation, XPS, SIMS

1. Introduction

Ions obtained from modern sources and used in various applied and basic studies are very diverse. Their list includes virtually all elements of the periodic table, including radioactive, positive and negatively charged ions with different charge multiplicity, and atomic, molecular, and polyatomic (cluster) complexes in both the ground and excited states. Ion beams are applied in micro- and nanotechnologies, spacecraft engines, ion-beam technologies in medicine, plasma heating in thermonuclear reactors, state-of-the-art analytical instruments, and many other areas. Ion sources are also very diverse: they are based on ionization of gaseous media by electrons and photons, chemical, surface, and field ionization, and plasma and radio frequency sources (the list can be continued). Unfortunately, the last monograph in Russian on the physics and technology of ion sources was published back in 1998 [1]. *Uspekhi Fizicheskikh Nauk* (*Physics-Uspekhi*), in the section ''Instruments and Methods of Investigation,'' partly compensates for the lack of information on this important branch of experimental physics. Recently, analytical reviews have been published on sources of negative ions [2] and electrohydrodynamic sources [3]. This review, which continues the topic of modern ion sources, is devoted to gas-dynamic sources of cluster ions. It covers gas cluster ion beams (GCIBs), i.e., charged complexes that include from tens to several thousand particles (atoms or molecules) held together by weak (~ 0.1 eV) van der Waals forces.

Although the phenomenon of gas condensation was known as early as the first half of the 20th century, the techniques to form intense directed flows of gas clusters only appeared with the emergence of gas-dynamic sources of molecular beams [4, 5]. Beams of gas clusters were obtained for the first time from a supersonic jet of easily condensing CO_2 and recorded using mass spectrometry [6, 7]. One of the first studies of the ionization of CO_2 clusters by an electron beam at an electron energy of 40–580 eV was carried out in [8]. Since the properties of matter in clusters differ from those of both their constituent particles and a continuous medium, gas clusters have long been the object of numerous basic studies.

Apparently, the first practical application of a gas-dynamic ion-cluster beam was described in [9], where a high-current source of hydrogen cluster ions with an equivalent ion beam current of up to 10 A and an energy of 1 MeV was developed for injection into a thermonuclear reactor. Cluster

A E Ieshkin [(1, a)], **A B Tolstoguzov** [(2, 3, 4, b)], **N G Korobeishchikov** [(5)], **V O Pelenovich** [(3)], **V S Chernysh** [(1)]
[(1)] Lomonosov Moscow State University, Faculty of Physics, Leninskie gory 1, str. 2, 119991 Moscow, Russian Federation
[(2)] Utkin Ryazan State Radio Engineering University, ul. Gagarina 59/1, 390005 Ryazan, Russian Federation
[(3)] Department of Physics and Key Laboratory of Artificial Micro- and Nano-structures of the Ministry of Education, Hubei Nuclear Solid Physics Key Laboratory and Center for Ion Beam Application, School of Physics and Technology, Wuhan University, 430072 Wuhan, China
[(4)] Centre for Physics and Technological Research (CeFITec), Dept. de Fisica da Faculdade de Ciencias e Tecnologia (FCT), Universidade Nova de Lisboa, 2829-516 Caparica, Portugal
[(5)] Novosibirsk State University, ul. Pirogova 2, 630090 Novosibirsk, Russian Federation
E-mail: [(a)] ieshkin@physics.msu.ru, [(b)] a.tolstoguzov@fct.unl.pt

Received 23 March 2021, revised 20 May 2021
Uspekhi Fizicheskikh Nauk **192** (7) 722 – 753 (2022)
Translated by M Zh Shmatikov

ions with an average size of 300 atoms/charge were formed by intense electron beam ionization of neutral hydrogen clusters with a size of $10^4 - 10^5$ atoms in a cluster. The first work on the use of gaseous cluster ions for surface treatment of various materials only appeared in the 1990s. A significant contribution in this area has been made by the groups of the Karlsruhe Institute for Nuclear Technology (Institut für Kernverfahrenstechnik, Karlsruhe, Germany) [10, 11] and the University of Kyoto (Japan) [12].

The fundamental difference between cluster ion beams and conventional (monoatomic) beams is the collective nature of the interaction of cluster ions with the target. When a cluster collides with a surface, several ten to several thousand of its atoms locally interact with approximately the same number of near-surface target atoms. In this case, nonlinear processes occur that cannot be described by known models. In addition, the possibility of independently varying not only the accelerating potential but also the size of gas clusters enables forming intense particle flows with a very low kinetic energy per cluster atom (at the level of units of eV and below), which is virtually unattainable in an atomic ionic beam. These features open a variety of areas where gas-dynamic cluster ion beams can be applied in practice, such as minimally invasive surface modification (sub-nanoscale smoothing and nanostructuring, chemical activation), near-surface implantation, and precision analysis (depth profiling).

Summarizing all of the above, it can be asserted with confidence that gas-dynamic sources of cluster ions are of great interest for both the development of modern technologies and the exploration of a wide range of basic scientific problems.

2. Formation of beams of accelerated cluster ions

Beams of accelerated gas cluster ions are formed in several stages. At the first stage, a flux of accelerated neutral clusters is obtained. These clusters are then ionized and accelerated to the required energy. After that, if required, mass selection is applied to separate cluster ions from the beam in the required mass range and subsequently focus them on the target. We now consider these steps one by one.

2.1 Formation of intense beams of neutral gas clusters

The main technique to obtain an intense flow of neutral gas clusters is the condensation of gas in the process of its adiabatic expansion through a nozzle into a vacuum chamber with reduced background pressure. Under such an expansion, the thermal energy of a gas at rest, which includes the kinetic energy of randomly moving particles (atoms or molecules) and the energy stored in internal degrees of freedom (for molecular gases), is effectively converted into the energy of directed translational motion. The mechanism of gas-dynamic cooling is implemented, in which the distribution of particle velocities in the flow is greatly narrowed, and the temperature of translational motion decreases [13]. The gas passes into an unstable state of super-saturation and, provided that the number of interatomic collisions is sufficiently large, its condensation with the formation of clusters becomes possible.

To date, a significant number of articles, reviews [14–18], and monographs [19–24] have been published, which provide a reasonable understanding of nonequilibrium physical processes that determine condensation during gas-dynamic outflow of gases and gas mixtures. For a complete description of such processes, it is necessary to specify the type of outflowing gas (in the form $\gamma = C_P/C_V$, i.e., the ratio of specific heat capacities, which is the adiabatic index for adiabatic outflow), its initial state (pressure P_0 and temperature T_0, which are stagnation parameters), the geometrical parameters of the nozzle (diameter of the critical section d_*, nozzle profile, length L_n, and diameter of the outlet section d_a), and the gas parameters in the ambient space (P_∞, T_∞).

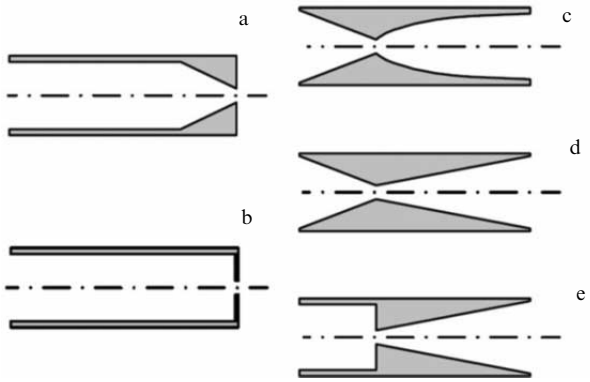

Figure 1. Shapes of axisymmetric nozzles used to create cluster beams: (a, b) sonic nozzles, (c–e) supersonic nozzles [20].

To form gas-dynamic (supersonic) beams, axisymmetric nozzles of various shapes are conventionally used, which can be divided into two large classes: sonic and supersonic (Fig. 1a, b). In sonic nozzles (in the simplest case, this is a hole in a wall, the thickness of which is less than the diameter of the hole), the outflow velocity reaches the speed of sound at the nozzle exit. The flow is further accelerated outside the nozzle in a free jet. The free expansion of the gas leads to a large angle of turn of the streamlines at the nozzle edge ($> 80°$ relative to the flow axis), a sharp drop in the local density of particles, and, as a result, a low probability of cluster formation. Supersonic nozzles always have an expanding part (diffuser), in which the flow is accelerated to supersonic speed. Gas particles in a flow limited by the nozzle walls undergo more collisions, which makes it possible to ensure a high efficiency of cluster formation.

Supersonic nozzles can have different shapes (Fig. 1c–e). The formation of clusters was shown to be primarily influenced not by the shape of the nozzle but by the opening angle of the diffuser [25–27]. Due to the greater ease of fabrication, conical nozzles are commonly used in cluster sources. To obtain clusters of maximal dimensions, nozzles with large length ($L_n \gg d_*$) and small opening angles ($\varphi \leqslant 10 - 20°$) are used. Under such conditions, the formation and growth of clusters are primarily localized inside the nozzle. In particular, simulation shows that the average size of clusters $\bar{N}$ and fraction of condensate q (fraction of molecules combined into clusters) already at the nozzle exit reach 2/3 of their limiting values in the far field of the flow (Fig. 2). However, a significant increase in the nozzle length is not rational due to the conservative nature of condensation (see below) and growth of the boundary layer on the internal walls of the nozzle.

If a gas outflows into a medium with a nonzero background pressure, a supersonic jet is formed with finite dimensions, which has a characteristic barrel-like shape

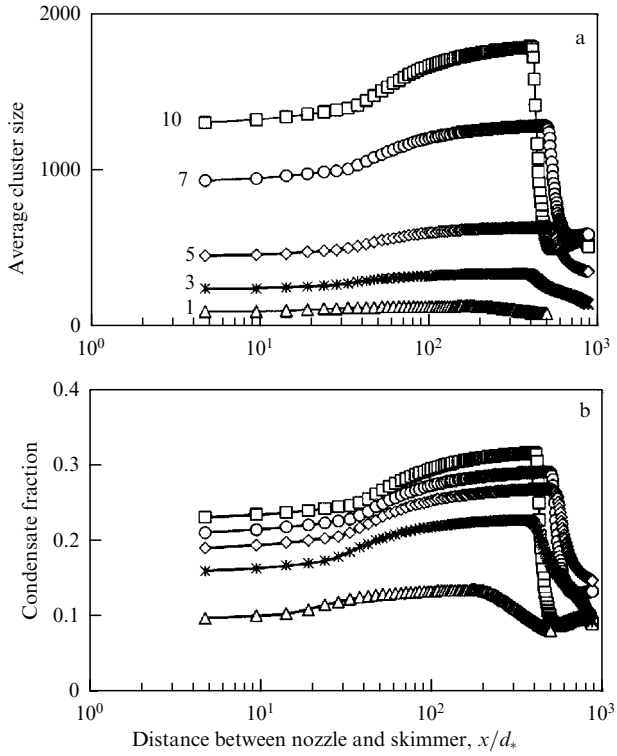

Figure 2. Axial profiles of the average cluster size $\bar{N}$ (a) and the condensate fraction q (b) in an argon jet at various stagnation pressures. Pressure values are shown in panel a in units of 10^5 Pa. Conical nozzle, $d_* = 0.2$ mm, $L_n = 17$ mm, $d_a = 3.8$ mm. Calculation results taken from [28].

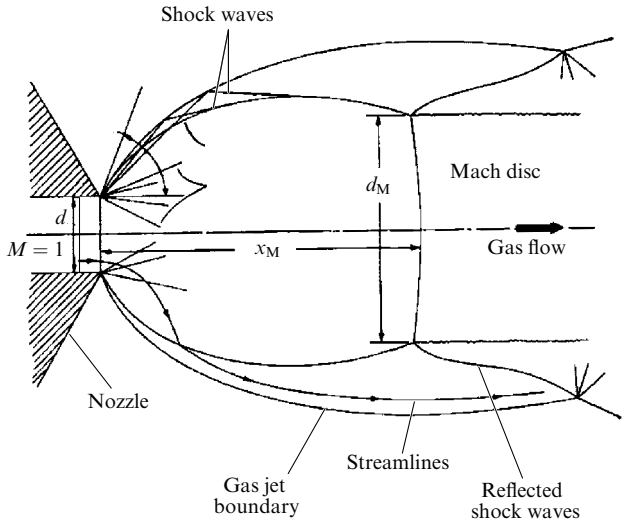

Figure 3. Structure of a gas jet flowing out of a sonic nozzle [31].

(Fig. 3). Since the formation of an intense flux of clusters requires a high local density in the expanding flow and, consequently, a high gas flow rate from the nozzle, regimes of underexpanded flow into the submerged space are realized. Under such conditions, the pressure at the nozzle outlet P_a exceeds that in the surrounding space P_∞ (the off-design degree $n = P_a/P_\infty > 1$) [29]. Lateral (hanging) shock waves and accompanying mixing zones (turbulence) determine the transverse dimensions of the jet. The jet is bounded along the flow axis by a central (direct) shock wave (Mach disk). In the shock waves, the deceleration of the outflowing gas and its

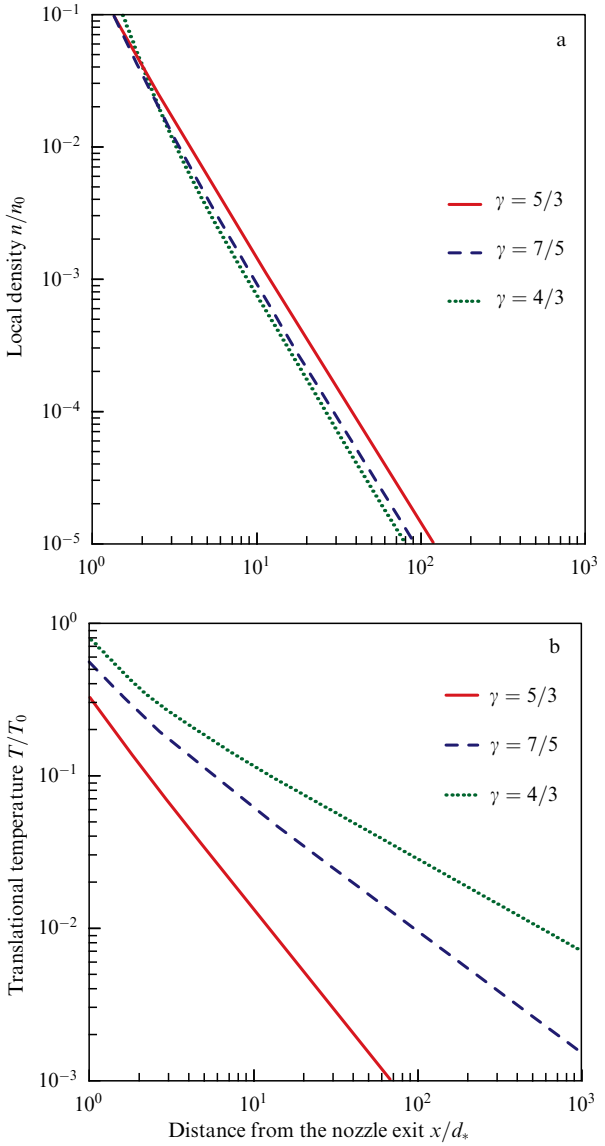

Figure 4. Distribution of density (a) and translational temperature (b) along the axis of a free jet in an isentropic outflow.

transition from supersonic to subsonic outflow occur. In the area limited by lateral and direct shock waves, the distribution of gas-dynamic parameters corresponds to a free radial outflow of gas into a vacuum and is well described by isentropic formulas:

$$\frac{T}{T_0} = \left(1 + \frac{\gamma - 1}{2} M^2\right)^{-1}, \qquad \frac{n}{n_0} = \left(1 + \frac{\gamma - 1}{2} M^2\right)^{-1/(\gamma-1)}. \tag{1}$$

The Mach number along the flow is determined using the empirical formula [30]

$$M = A\left(\frac{x - x_0}{d}\right)^{\gamma-1} - \frac{1}{2}\left(\frac{\gamma+1}{\gamma-1}\right)\left[A\left(\frac{\gamma+1}{\gamma-1}\right)^{\gamma-1}\right]^{-1}, \tag{2}$$

where A and x_0 are constants depending on γ.

Figure 4 shows the distributions of translational temperature and gas density as a function of the distance to the nozzle

for different values of γ. It can be seen that, for all gases, the gas density decreases inversely proportional to the square of the distance from the nozzle exit: $n \sim 1/(x/d)^2$. Relaxation of the internal degrees of freedom of molecules leads to a less intense cooling of the supersonic flow and, conversely, to a greater decrease in its local density. Thus, all other conditions being equal, the outflow of gases with a large adiabatic index facilitates the formation of clusters.

Clusters formed as a result of condensation are partially or completely destroyed due to collisions with decelerated particles during the transition through shock waves. Under the conditions corresponding to Fig. 2, this occurs at a distance $x/d_* \approx 400-600$. Therefore, the cluster beam, like the molecular beam, is formed from the inner unperturbed region of the supersonic jet (silent zone).

The cluster beam is separated from the supersonic flow using a conical diaphragm (skimmer). When a skimmer is introduced into a supersonic flow, a shock wave inevitably forms on the outer surface of the skimmer. Therefore, to avoid scattering the beam by the outgoing shock wave, the leading edges of the skimmer are made with a minimum thickness, and the outer angle of the skimmer is usually $35^\circ - 50^\circ$ [32, 33]. The diameter of the skimmer inlet determines the intensity of the produced beam (see below) and the pressure in the post-skimmer chamber. It was shown that the influence of skimmer interaction on the intensity of the molecular beam can be eliminated under the condition $Kn_{sk} > 1$, where $Kn_{sk} = \lambda/d_{sk}$ is the Knudsen number for the skimmer, λ_{sk} is the mean free path at the entrance to the skimmer, and d_{sk} is the diameter of the skimmer hole [34–36]. Therefore, the skimmer is usually positioned in such a way that its inlet is located in the far field of the jet flow in front of the Mach disk.

To estimate the longitudinal size of the jet, i.e., the distance from the nozzle exit section to the Mach disk x_M, several empirical formulas were proposed that relate the jet length to the flow parameters at the nozzle exit [31, 37]. However, most frequently used is the empirical dependence [30]

$$\frac{x_M}{d} = 0.67\sqrt{\frac{P_0}{P_\infty}}. \tag{3}$$

For sonic nozzles, the diameter of the outlet section d is taken as a characteristic dimension $d = d_a = d_*$, while, for supersonic nozzles, the diameter of the critical section is used to this end. The mass flow rate of gas from the nozzle G_m depends on the initial parameters of the gas and the critical section area S_*:

$$G_m = \left(\frac{2}{\gamma+1}\right)^{(\gamma+1)/2(\gamma-1)} \sqrt{\frac{\gamma\mu}{RT_0}} P_0 S_*, \tag{4}$$

where R is the gas constant, and μ is the molar mass of the gas.

Background pressure P_∞ in the chamber where the nozzle is installed is determined by the flow rate of the working gas from the nozzle G (Pa m^3 s^{-1}) and the performance of the vacuum pump used S: $P_\infty = G/S$. The gas flow rate usually ranges from several ten to hundreds of sccm (standard cubic centimeters per minute, i.e., the volume of gas is taken under normal conditions). It is easy to estimate that, at a constant gas flow rate from the nozzle of 100 sccm and a characteristic pumping speed of 1000 l s^{-1}, pressure P_∞ is set at a level of 1.25×10^{-3} Torr. According to (3), at a characteristic stagnation pressure of $P_0 = 3$ bar and diameter of the critical section $d_* = 50$ μm, the longitudinal size of the jet is $x_M \approx 45$ mm.

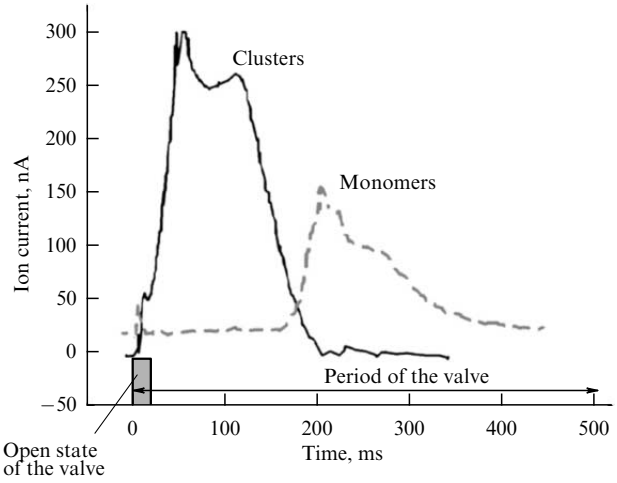

Figure 5. Signal of the cluster and atomic components of an ion beam in the pulsed operating mode of a source with a buffer volume [48].

To obtain an intense cluster beam, a large flow rate of the working gas from the nozzle should be ensured. Therefore, to maintain an acceptable background pressure in the vacuum chamber, it is necessary to use a high-performance evacuation system. One way to reduce the load on the pumping system is to apply a pulsed flow regime [38, 39]. Clusters are formed in this case during a time interval limited by the time of existence of a stationary flow [40, 41]. To form pulsed jets, gas valves are usually used with a pulse duration from several μs to several ms and a frequency of up to several kHz [42–44]. Cluster ion beam setups also use pulsed gas outflow modes [45–47]. However, pulsed sources lead to a significant (inversely proportional to the duty cycle of the cluster ion current pulses) increase in the exposure time needed to attain high target bombardment doses.

Specific features of the operation of the source of cluster ions in the presence of a buffer volume between the pulsed valve and nozzle are described in [46, 48]. Signals of cluster and atomic ion current and a time diagram of the process are shown in Fig. 5. During the open state of the pulse valve, the working gas quickly fills the buffer volume, and the formation of a cluster flow begins. The outflow of gas through the nozzle is relatively slow. As it flows out, the pressure of the working gas in the buffer volume decreases and, accordingly, the size of the Mach barrel decreases. Starting from the moment when the Mach barrel boundary ceases to reach the skimmer, the clusters are no longer registered, since they are destroyed when passing through the shock wave; however, the signal of the atomic component of the ion beam increases.

To determine the geometric characteristics of the gas flow at the nozzle outlet, visualization methods are applied that use shadow photography [49] or excitation of luminescence by an electron flow [50]. In studies [51, 52], the structure of the gas flow under the conditions of cluster ion formation and interaction with a skimmer was visualized in a glow discharge. This method is easier to implement.

When gases flow out of sonic and short supersonic nozzles, the transverse dimensions of the jets are comparable to their longitudinal dimensions (Fig. 6a). If long supersonic nozzles are used, the angle of turn of the streamlines at the nozzle exit is significantly limited. As a result, the transverse dimensions of the jet are significantly reduced, the Mach disk is absent, and the longitudinal dimension is limited by the

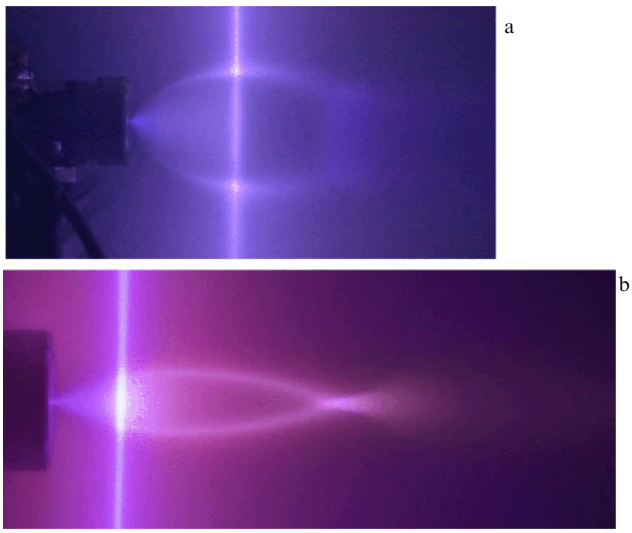

Figure 6. (a) Nitrogen jet behind a sonic nozzle at $d_* = 2$ mm, $P_0 = 980$ kPa, $T_0 = 300$ K. (b) Nitrogen jet behind a supersonic nozzle at $d_* = 0.256$ mm, $L_n = 3.55$ mm, $P_0 = 400$ kPa, $T_0 = 300$ K, $P_\infty = 4$ Pa. Photometry data with excitation by an electron beam; glow intensity shows the gas density distribution in the flow [54].

X-shaped configuration formed by the closing of the lateral shock waves (Fig. 6b) [50–53].

The conservative character of condensation, which is exhibited in the finite value of the fraction of condensate attainable with a jet outflow of gases, is due to thermodynamic and kinetic limitations. Gas condensation is known to be accompanied by the release of additional energy (the heat of condensation) into the supersonic flow. In a free jet, this results in an increase in the limiting velocity of the outflow and the longitudinal and transverse dimensions of the jet [31, 54]. As a result, the local density of the gas decreases, which leads to the limitation of collisions between monomers and clusters, as well as condensation process as a whole. Under real conditions, the fraction of molecules combined into clusters, q (the fraction of condensate), does not usually exceed 10% of the total gas flow rate from the nozzle. However, due to gas-dynamic separation [55], the formed heavy clusters are concentrated in the paraxial region of the jet. As a result, the proportion of condensate on the jet axis can be as high as 30–35% (see Fig. 2). The release of condensation heat inside the nozzle leads to an increase in the local temperature of the flow, which in turn limits the increase in cluster sizes and the proportion of condensate for an arbitrarily large increase in stagnation pressure.

To describe gas condensation in supersonic flows, Hagena proposed a similarity law based on the principle of 'corresponding jets' [38, 56–58]. The dimensionless similarity parameter Γ^*, later called the Hagena parameter, can be used to compare condensation in jets of different gases behind nozzles of different geometries. The parameter Γ^*, which depends on the type of gas, gas parameters in the source (P_0 and T_0), and nozzle geometry (in terms of the equivalent diameter d_{eq}), for an axisymmetric flow has the following form [59]:

$$\Gamma^* = kP_0 d_{eq}^{q} T_0^{q\left[(f-2)/4-\gamma/(\gamma-1)\right]}, \tag{5}$$

where k and q are empirical coefficients depending on the type of gas and f is the number of active degrees of freedom of gas particles. It should be taken into account that, during the expansion of gases at room temperature ($T_0 \sim 300$ K), only some internal (rotational and vibrational) degrees of freedom of molecules are active. For monatomic gases, it was found that $q = 0.85$, from which follows the well-known formula

$$\Gamma^* = kP_0 d_{eq}^{0.85} T_0^{-2.29}, \tag{6}$$

where the pressure is expressed in millibars and the nozzle diameter, in micrometers. The values of the coefficient k have been determined for all noble and some molecular gases [60] (Table 1).

For sonic nozzles, the equivalent diameter is equal to the critical one. For conical supersonic nozzles, the following relationship is used:

$$d_{eq} = \frac{c(\gamma) d_*}{\tan\alpha}, \tag{7}$$

where α is the half-angle of the nozzle cone. For an axisymmetric flow, the constant $c(\gamma)$ is equal to 0.736, 0.866, and 0.986 for monatomic ($\gamma = 5/3$), diatomic ($\gamma = 7/5$), and triatomic ($\gamma = 9/7$) gases, respectively [20].

A beam formed from a supersonic jet of condensing gas contains both monomers and clusters of various sizes. Therefore, the total intensity of a gas-dynamic cluster beam at the entrance to the skimmer I [mol. cm^{-2} s^{-1}] is the sum of the intensities of the monomeric and cluster components [24]:

$$I = I_{mono} + I_{clust} \cong n_{sk} U d_{sk}^2 S^2 \left[(1-q) + q\bar{N}\right], \tag{8}$$

where n_{sk} is the numerical value of the flux density at the skimmer inlet, U is the directional flow velocity, d_{sk} is the diameter of the skimmer inlet, S is the velocity ratio associated with the Mach number, $S = U(m/2kT)^{0.5} = M(\gamma/2)^{1/2}$, q is the fraction of the condensate, $\bar{N}$ is the average number of molecules in a cluster (average cluster size), and m is the mass of the molecule.

It is known that, under conditions of free molecular expansion, in a molecular beam consisting of particles of different masses, the Mach focusing effect is observed, which results in enrichment of the beam axis with heavy particles [61]. For a cluster beam downstream from the skimmer, the on-axis intensity decreases monotonically as a result of beam broadening (an increase in its diameter). Beam broadening Δ is determined by the velocity ratio of the flow: $\Delta \sim 1/S$. Since $S_{clust} = \sqrt{N} S_{mono}$, the monomer component of the beam is broadened into a larger solid angle. The fraction of condensate Q on the beam axis is always greater than that in the jet:

$$Q = \left[1 - \frac{1}{N}\left(1 - \frac{1}{q}\right)\right]^{-1}. \tag{9}$$

Table 1. Values of coefficient k for various gases [60].

Gas	H_2	D_2	O_2	CO_2	CH_4	He	Ne	Ar	Kr	Xe
k	184	181	528	1400	3660	2360	3.85	1650	2890	5500

As a result, at a large distance behind the skimmer, $L \gg d_{sk}$, the fraction of condensate in the beam can be more than 90% [59].

To estimate average cluster size $\bar{N}$, several empirical dependences have been proposed. If the value of Hagena parameter Γ^* lies in the range of 350–1800, the average size of the formed clusters is described by the empirical formula [62]

$$\bar{N} = 38.4\left(\frac{\Gamma^*}{1000}\right)^{1.64}. \qquad (10)$$

For the conditions $\Gamma^* > 1800$, two empirical formulas are available:

$$\bar{N} = 33\left(\frac{\Gamma^*}{1000}\right)^{2.35} \text{ [38]},$$

$$\bar{N} = \exp\left[-12.58 + 3.51(\ln\Gamma^*)^{0.8}\right] \text{ [63]}. \qquad (11)$$

Depending on the value of parameter Γ^*, which can be controlled in the easiest way by changing the pressure P_0, several stages of condensation are distinguished. At low stagnation pressures ($\Gamma^* < 200$), condensation does not occur in the jet due to insufficient local gas density in the expanding flow. The beam intensity increases in proportion to pressure P_0 (Fig. 7). At the initial stage of condensation at $\Gamma^* > 200$, a significant number of Ar_2 dimers emerge in the supersonic flow. The subsequent development of gas condensation is accompanied by an increase in the average size of clusters. The heat of condensation released into the flow results in a decrease in the intensity of the cluster beam. Mass condensation causes an explosive increase in the intensity of cluster beam I and the mass fraction of condensate q. At $\Gamma^* \geqslant 1800-2000$, the flow passes to the stage of developed condensation, at which the growth in the fraction of condensate slows down, while the increase in the average size of clusters, on the contrary, accelerates. Apparently, this leads to a decrease in cluster flux density J, expressed in the units [cluster $\text{cm}^{-2}\ \text{s}^{-1}$].

To obtain clusters of weakly condensing gases, the outflow of binary gas mixtures is used, in which a heavy working gas is added as a small admixture to a light carrier gas, for which helium is usually used, the probability of condensation of which is very small. When a sufficient number of collisions between helium atoms and impurity gas molecules is attained, both components of the flow acquire almost the same velocities and translational temperatures. The dynamics of the mixture outflow are determined by the average value of the adiabatic exponent: $\overline{\gamma} = c_l\gamma_l + c_h\gamma_h$, where c_l, γ_l and c_h, γ_h are the concentrations and adiabatic exponents of the light and heavy components. If the proportion of impurities is small, it is the carrier gas that sets the rate of flow cooling, which is close to the isentrope of a monatomic gas, thus providing a high efficiency of impurity component condensation. In addition, helium atoms effectively remove the heat of condensation, stabilizing the formed clusters. As the impurity concentration increases, the outflow dynamics shift closer to the impurity isentrope, which deteriorates the conditions for condensation. The optimal concentration for obtaining the maximum intensity of the cluster beam depends on the properties of the impurity gas (adiabatic exponent, molecular mass) (Fig. 8). For well-condensing gases (Ar, N_2O), dilution with helium results in suppression of condensation, while, for CO_2, it only yields a slight increase in intensity. The use of other monatomic gases (for example, argon) instead of helium can lead to the formation of mixed clusters, including the core–shell structure [64, 66–68]. As to the formation of mixed clusters, of interest as well is the possibility of capturing atoms of a different sort only after cluster formation [69] and the transition to the core–shell structure under the effect of external perturbations [70].

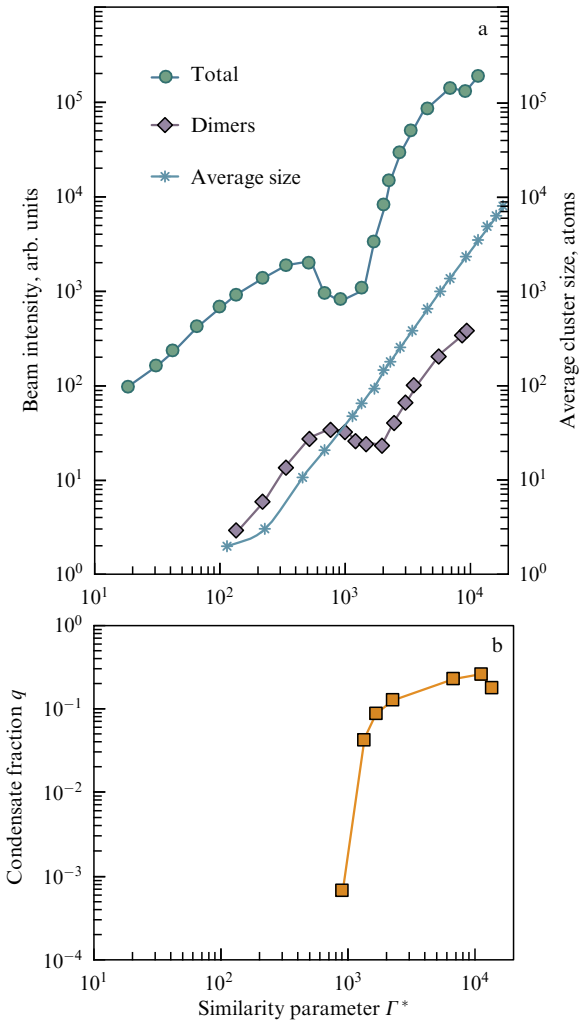

Figure 7. (a) Total intensity of the cluster beam, the intensity of the dimer component (Ar_2), and the average size of argon clusters as functions of condensation similarity parameter Γ^*. (b) Mass fraction of the condensate in an argon jet as a function of parameter Γ^* [64, 65].

2.2 Diagnostics of flows of neutral clusters

The key parameters of gas cluster flows are the average cluster size $\bar{N}$, their numerical density n_{cl} or flux density J_{cl} [cluster $\text{cm}^{-2}\ \text{s}^{-1}$], and the ratio of the clustered and monomeric components (mass fraction of condensation q). At present, various experimental methods are used to diagnose gas cluster flows, most of which are aimed at measuring the average size of clusters.

The widely used method of Rayleigh scattering, based on recording the intensity of coherent radiation elastically scattered by clusters, is absolutely nondestructive [26, 72–74]. However, it does not allow direct determination of the absolute sizes of clusters, since the intensity of the scattered laser signal I_R depends not only on the average size $\bar{N}$ of

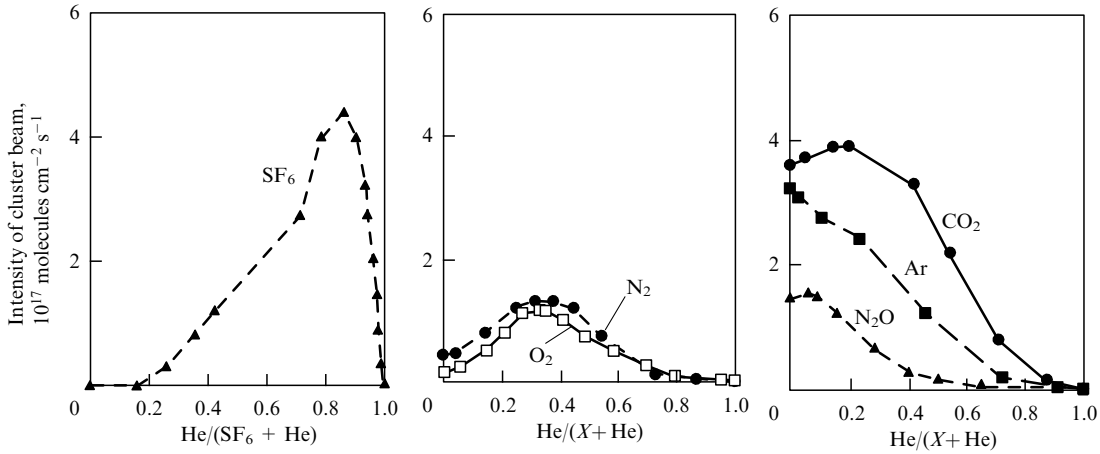

Figure 8. Intensity of a cluster beam formed from a supersonic jet of binary gas mixtures [71].

clusters but also on their density:

$$I_R \sim c\bar{N}^{\,2} n_{cl}\,, \tag{12}$$

where c is a constant that depends on the type of gas and experimental conditions. Therefore, to determine the absolute characteristics of cluster fluxes, it is necessary to use additional estimates or assumptions or apply a combination of various optical methods, for example, Raman and Rayleigh scattering [75], Rayleigh scattering and interferometry [76–78], or Rayleigh scattering and absorption spectroscopy [79]. Due to the small absolute values of the scattering cross sections, such methods can primarily determine the sizes of large clusters. Such measurements require sophisticated, highly sensitive equipment.

Various spectrometric methods are also used to determine the average size of gas clusters: X-ray photoelectron spectroscopy (XPS) [80–82], infrared spectroscopy [83, 84], and high-energy electron diffraction [85, 86]. Diagnostic methods are known, which are based on the interaction of a cluster beam with a buffer gas, leading to elastic scattering, cluster beam broadening [87], the capture of buffer particles (pickup techniques), and changes in the average velocity of beam particles [88], as well as the method of scattering of a crossed helium molecular beam by a cluster beam [62]. Such methods are based on the destruction of a cluster beam, which is not always acceptable. Unfortunately, for each gas under study, it is required to develop a special model that connects the registered physical quantity with the actual sizes of clusters of this gas. As a rule, such models contain empirical constants, the determination of which requires complex calibration procedures. In this case, the scattering cross section often depends not only on the size but also on the structure of the clusters.

Recently, a new method has been developed to determine the average sizes of neutral gas clusters, which is based on measuring the transverse profile of the total intensity of the cluster beam at a fixed distance behind the skimmer. The method proposed is applicable for diagnosing beams of clusters of any pure gases of medium (50–100) and large (100–2000) dimensions and, under certain conditions, gas mixtures. This method does not require the development of special models or the determination of additional empirical constants for different gases [59, 89].

Figure 9 shows the average sizes of argon clusters measured by various methods, depending on the similarity

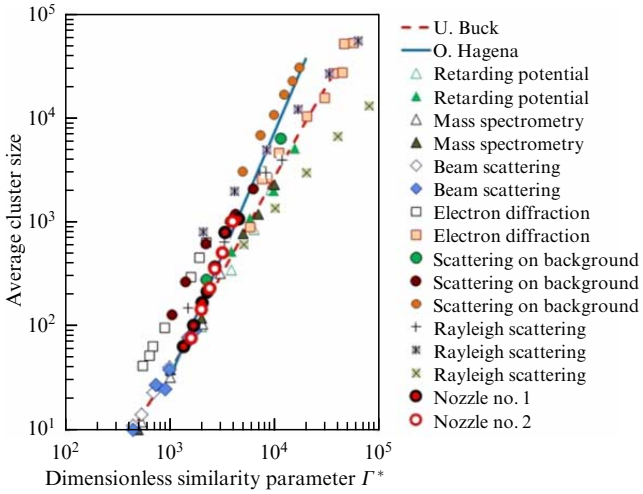

Figure 9. Comparison of argon cluster sizes determined using various diagnostic methods vs. condensation similarity parameter Γ^* [59].

parameter Γ^*. In the experiments, conical nozzles of various geometries (filled symbols) and sonic nozzles (unfilled symbols) were used. In the same plot, the curves show the dependences obtained using the known empirical dependences [38] and [62]. It can be seen that, at a fixed value of Γ^*, a fairly large dispersion of results for different methods is observed, which may be a consequence of systematic measurement errors or the contribution of unaccounted for nozzle geometry features.

To measure mass (size) distribution clusters, time-of-flight (TOF) mass spectrometry [90, 91] and the retarding potential method are usually employed. Time-of-flight diagnostics are based on measuring the time t required for ions with different masses, but accelerated by the same voltage U_{acc}, to pass through the drift space L. To this end, a short ion pulse is formed at the entrance to the drift space, for example, using deflecting plates, and its shape at the end of the drift space is registered. The ion mass M is determined from the formula

$$M = 2ZeU_{acc}\frac{t^2}{L^2}\,. \tag{13}$$

The retarding potential method is based on the fact that the velocity distribution of neutral clusters in a cluster beam is

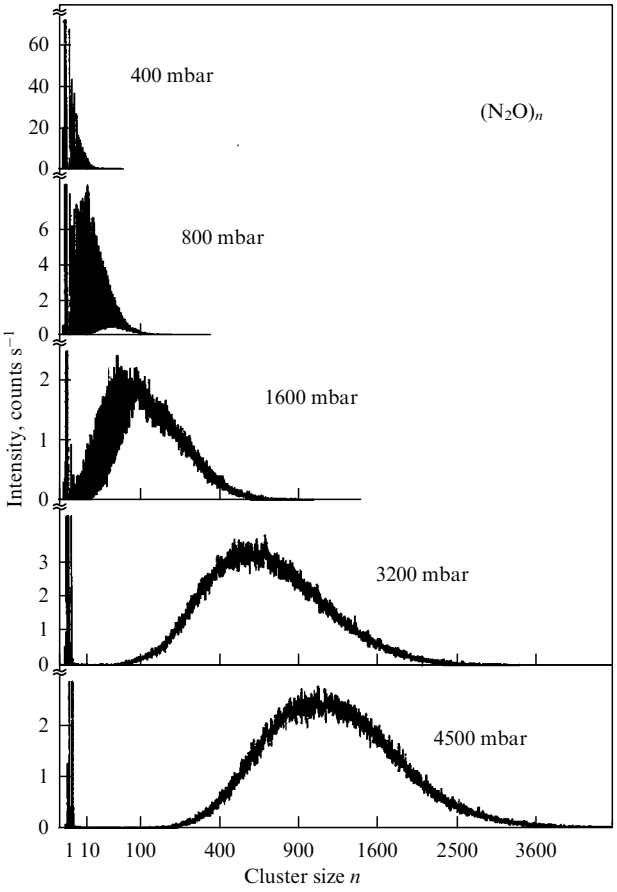

Figure 10. Size distributions of gas clusters at various stagnation pressures P_0 measured using the time-of-flight technique [94].

rather narrow and close to the hydrodynamic flow velocity. If the ion velocities do not change after ionization, the kinetic energy of a cluster ion is only determined by its mass (size). By changing the value of the retarding potential in the space before the ion detector, it is possible to determine the size distribution of clusters [25, 92, 93].

The main advantage of time-of-flight diagnostics and the retarding potential method is the virtually unlimited range of measured masses. However, both methods are based on the ionization of neutral clusters. A significant drawback is the probable fragmentation of clusters that occurs during their ionization (see Section 2.3), which results in a decrease in their size and, thus, a distortion of the true distribution function. Moreover, the time-of-flight spectrum is analyzed based not on the mass of the ions as such but on the mass-to-charge ratio. Given that multiply charged cluster ions can be formed, this circumstance can also be a serious problem.

The characteristic shape of the size distribution of clusters at various stages of condensation is shown in Fig. 10 using nitric oxide as an example [94]. The distribution functions have been obtained using time-of-flight diagnostics. It can be seen that at the initial stage of condensation (400 mbar) the distribution has the form of a unimodal function with an intensity maximum at the dimer mass. Upon passing to the mass condensation stage, the distribution function transforms into a bimodal one. With a further increase in the stagnation pressure P_0, both the average cluster size and the width at half height of the cluster distribution function increase.

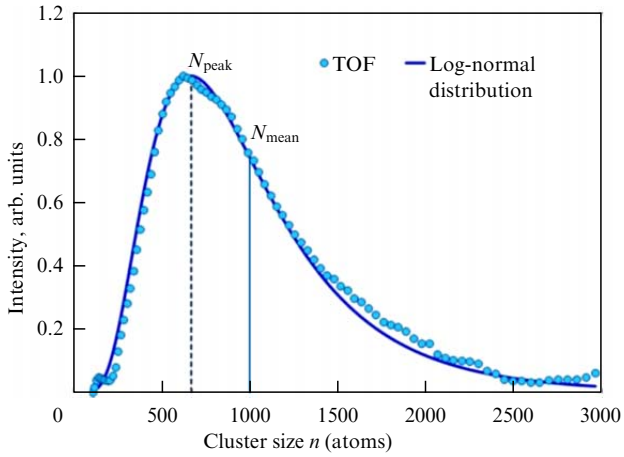

Figure 11. Approximation of the size distribution of clusters by a log-normal function [98].

The size distribution of gas clusters is well approximated by a log-normal function [95–97]:

$$f_n = \frac{1}{\sqrt{2\pi}n\sigma}\exp\left(-\frac{(\ln n-\mu)^2}{2\sigma^2}\right), \qquad (14)$$

where μ and σ are fitting coefficients. In this case, it is necessary to distinguish between the average size of clusters, defined as $\bar{N} = \exp(\mu+\sigma^2/2)$, and the most probable size N_{peak} (Fig. 11).

Measuring the mass fraction of condensate q in a supersonic gas flow is a rather complicated practical problem, since it requires establishing the absolute values of both the cluster and monomer components. In experiments, combinations of complementary methods are used to this end, such as measuring the refractive index of a jet using femtosecond-resolution holography [99], direct/backward Mie scattering, and optical imaging and interferometry [100].

To determine the intensity of a beam of gaseous clusters, a rather simple method is known, which based on measuring the overpressure that arises due to beam deceleration in a small sensor [59]. The overpressure P_{beam} is the result of the balance of the incoming and outgoing flows. The mass flow G_{in} of a cluster beam consisting of clusters and monomers with densities n_{cl} and n_1, respectively, which flows into the sensor can be estimated as

$$G_{in} = (n_{cl}N + n_1)S_{in}U \quad [\text{mol. s}^{-1}], \qquad (15)$$

where S_{in} is the area of the inlet and U is the hydrodynamic velocity of the beam. Gas clusters are destroyed in colliding with the walls inside the sensor. The number of collisions of molecules with walls inside the sensor w can be estimated from the relation $w = v\tau/D$, where τ is the time constant of the sensor, D is the characteristic size of the sensor, and v is the average particle velocity. For a free molecular outflow from a volume V through a hole with area S, the time constant is determined from the relation $\tau = 4V/vS$. It is easy to estimate that, for the characteristic size of the sensor $D = 5$ cm and the area of the inlet $S = 0.5$ cm^2, the number of collisions of molecules with the walls inside the sensor is $w \sim 10$. Apparently, under such conditions, all clusters inside the sensor are completely fragmented, and the flow leaving the sensor consists of monomers moving at an average speed that

corresponds to the temperature of the sensor walls T_{det}:

$$v = \sqrt{\frac{8kT_{\text{det}}}{\pi m}}. \quad (16)$$

Then, the outflowing free molecular flow G_{out} is determined as

$$G_{\text{out}} = \frac{1}{4} n_{\text{beam}} v S_{\text{out}}, \quad (17)$$

where n_{beam} is the equilibrium density of the gas in the sensor and S_{out} is the area of the outlet. If the incoming and outgoing flows pass through the same hole ($S_{\text{in}} = S_{\text{out}}$), the total (mass) intensity of the cluster beam I_{total} can be estimated as follows:

$$I_{\text{total}} = \frac{1}{4} \frac{P_{\text{beam}} v}{kT_{\text{det}}} = \frac{P_{\text{beam}}}{\sqrt{2\pi m k T_{\text{det}}}} \ [\text{mol. cm}^{-2}\ \text{s}^{-1}]. \quad (18)$$

Finally, for the regime of well-developed condensation, when, as indicated above, the intensity of the cluster component exceeds 90%, knowing the average cluster size $\bar{N}$, it is possible to estimate the cluster flux density $J_{\text{cl}} \approx I_{\text{total}}/\bar{N}$.

To describe the formation of gas clusters in supersonic flows, various numerical simulation methods are also used, which are based on calculations of the gas dynamics of the outflow and various condensation models. Numerical simulation potentially makes it possible to describe in detail the space-time distributions of the main parameters of a cluster flow both inside supersonic nozzles of various geometries and in a free jet [78, 101–106]. However, due to the absence of reliably known values of the model constants, the condensation of only a limited number of working gases can be simulated. In addition, such models usually fail to take into account accompanying perturbing processes, including the influence of background gas and skimmer interaction [52].

2.3 Ionization of neutral clusters

Various methods of ionization of gas clusters are known: photoionization [91], ionization during passage through a barrier or glow discharge [107], and ionization by an electron beam. The last method, first of all, is easy to implement, and, moreover, the choice of the energy of ionizing electrons and their current density enables accurate control of the properties of the flow of charged clusters.

One of the possible implementation options for an ionizer is shown in Fig. 12a [108]. The flow of clusters propagates along the axis of the system. Electrons emitted by hot tungsten cathodes are accelerated by an electric field between the external electrode and anodes and enter the ionizer cavity. The secondary electrons knocked out by them from the walls of the anodes compensate for the positive space charge of ionized clusters, which reduces their Coulomb repulsion and makes it possible to suppress losses on the path to the accelerating gap.

In an alternative setup (Fig. 12b [46]), the cathode is located between the outer electrode and the mesh cylindrical anode with high transparency. In this case, the electrons move along quasi-periodic trajectories, repeatedly passing through the ionization region, which makes it possible to use them more efficiently. Another way to increase the ionization efficiency of neutral clusters, described in [109] (Fig. 12c), is to use an electron flow coaxial with the cluster flow.

The disadvantage of the above designs is that the current of electrons and their energy cannot be varied in a wide range independently. This possibility could be provided by an additional mesh electrode, which sets the potential of the ionization region, regardless of the electric field in the emission region.

The need for precise control of the electron current and energy is due to the regularities of cluster beam ionization. The change in the mass spectrum of cluster ions depending on the ionization conditions is shown in Fig. 13. With an increase in the energy of ionizing electrons to values that greatly exceed the first ionization potential, the average size of cluster ions decreases due to the destruction of some clusters by such electrons. An increase in the current of ionizing electrons can also result in a decrease in the average size of cluster ions due to the destruction of clusters. In addition, with an increase in energy or current, the probability of multiple ionization of clusters increases. Since all conventional methods to measure the mass composition of an ion beam make it possible to determine not the mass of ions directly but rather the mass-to-charge ratio, the emergence of multiply charged clusters in the beam is also accompanied by a shift in the mass spectrum to lower masses.

Another effect leading to a real decrease in the size of clusters is due to the Coulomb destruction of multiply charged particles. The destruction of a multiply charged cluster occurs if the energy of the Coulomb repulsion of charges exceeds the binding energy of atoms in the cluster. Consequently, clusters of large sizes can remain stable at a higher multiplicity of their charge, so there is a certain critical cluster size $N(Z)$, starting from which clusters A_N^{+Z} can exist.

The critical sizes of clusters of some gases are presented in Table 2. Independent measurements of the average charge, mass, and energy of argon cluster ions showed that, with an average size of 10,400 atoms, the average charge of a

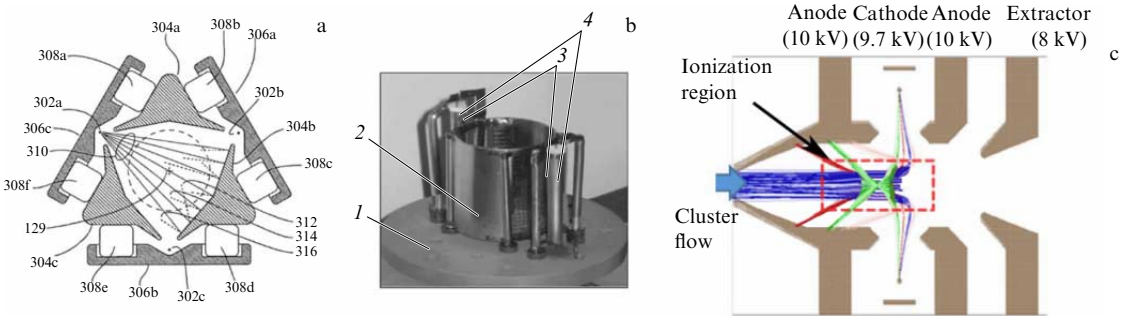

Figure 12. Various versions of the ionizer design. (a) 129 — beam axis, 302 — cathodes, 304 — anodes, 306 — external electrodes, 308 — insulators, 310 — ionizing electrons, 312, 314, 316 — secondary electrons; (b) *1* — ceramic base, *2* — cylindrical anode, *3* — emitting region of cathodes, *4* — indirectly heated cathodes. (c) Simulation of electron trajectories in a source with coaxial flows of clusters and electrons.

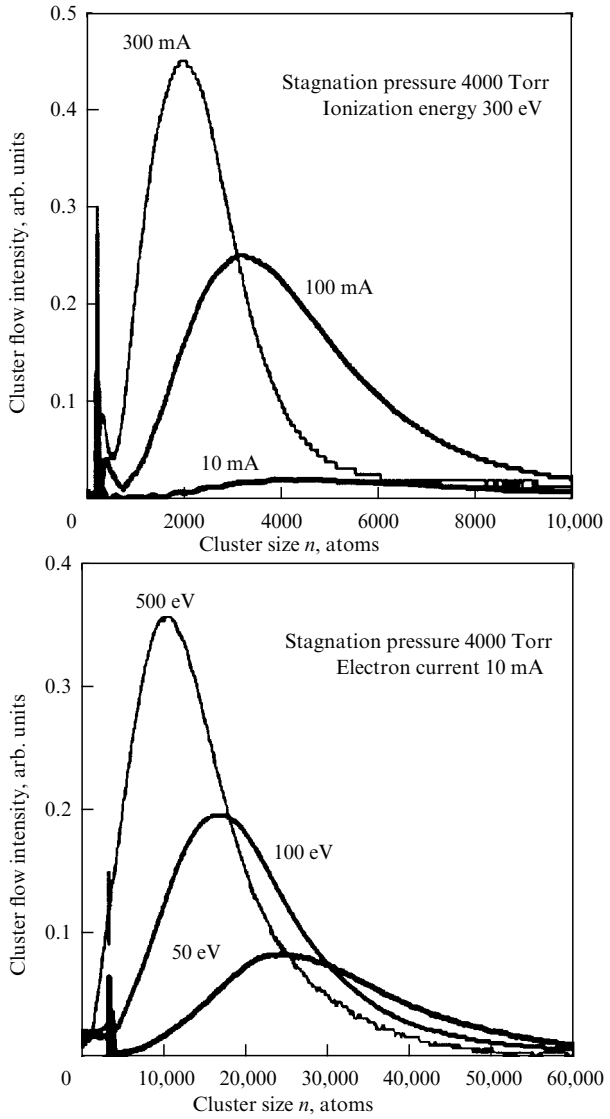

Figure 13. Mass distribution of cluster ions for various energies of ionizing electrons and ionization currents [110].

multiplicity of clusters is 3.2 [111]. In study [112], the distribution of cluster ions over the charge multiplicity was determined by measuring the sizes of craters produced by single accelerated clusters on the surface of silicon oxide. With an energy of ionizing electrons of 200 eV and an average cluster size of 3000 atoms, the average cluster charge was 2.1, and the maximum charge was 7.

Table 2. Critical size of cluster ions N as a function of their charge Z [14, 113, 114].

	$Z = 2$	$Z = 3$	$Z = 4$
$(Ar)_N^{+Z}$	92	226	—
$(Kr)_N^{+Z}$	69	156	264
$(Xe)_N^{+Z}$	54	115	209
$(N_2)_N^{+Z}$	100	216	—
$(CO_2)_N^{+Z}$	45	109	216

Passing through the ionizer, the clusters move by inertia, thus reaching the accelerating gap. In accelerators of gas cluster ions, a positive voltage U_{acc}, which is usually 1–30 kV, is applied to the ionizer, while the output electrode of the accelerating gap is at ground potential. On the whole, as the accelerating voltage increases, the current of accelerated cluster ions increases [115], although this dependence, generally speaking, is nonmonotonic (Fig. 14a). The specified configuration of the electrodes corresponds to the optimal accelerating voltage, which provides the lowest divergence of the ion beam combined with a high efficiency of their extraction from the ionization zone. The trajectories of cluster ions in the beam calculated using the SIMION software package [116] for various shapes of accelerating electrodes and voltages across them are shown in Fig. 14b [117].

An accelerated beam of cluster ions is focused using conventional electron-optical systems, most often based on single electrostatic Einsel lenses. Depending on the problem explored using the source, focusing is possible onto a region with a diameter of several micrometers (for use in scanning analytical techniques) [119, 120] or, conversely, onto a spot on the target surface with a diameter of several millimeters or even centimeters (for surface modification by cluster ions) [121, 122]. In addition, in some cases, scanning of the ion beam over the target surface is required, for example, to obtain micrograms in the local secondary ion mass spectrometry (this issue is discussed in more detail in Section 3.2.1).

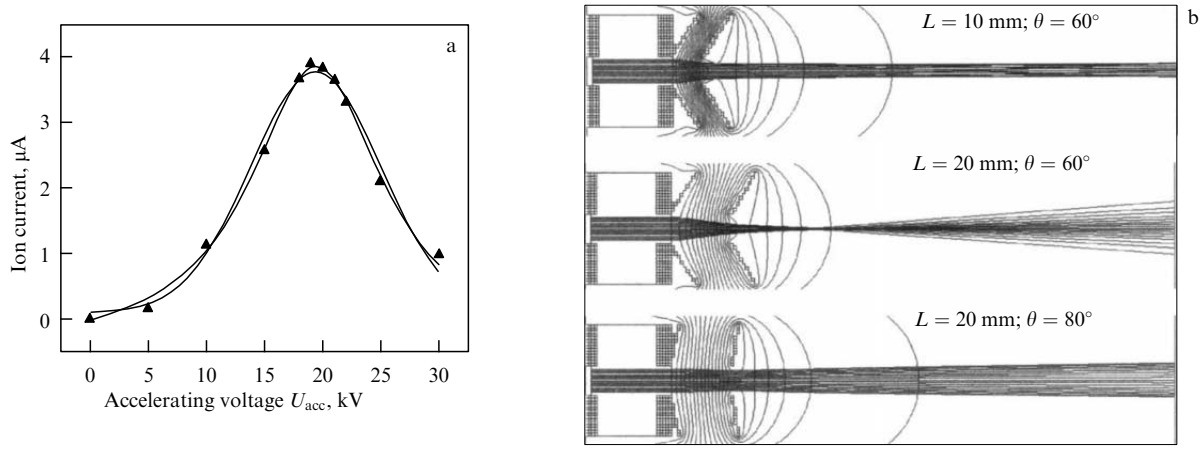

Figure 14. (a) Dependence of cluster ion beam current on accelerating voltage [118], (b) calculated trajectories of cluster ions for various electrode shapes: L is the distance between electrodes, θ is the opening half-angle [117].

This is achieved either by deflecting the beam from the axis using an electric field created by pairs of deflecting plates or by moving the target itself in a setup with a stationary ion beam. The latter method, in particular, is necessary when processing large-area targets, since the beam deviation from the axis over long distances can lead to a change in the beam diameter and the emergence of various aberrations. In addition, the angle of incidence of ions on different areas of the target can vary significantly.

Accelerated cluster ions feature a wide mass distribution, which is determined by both the initial distribution of neutral clusters and the ionization conditions. During the operation of the source of cluster ions, the mass distribution of clusters can be controlled by adjusting the pressure and temperature of the working gas at the nozzle inlet. In addition, this distribution is affected to a certain extent by the values of the current and energy of electrons in the ionizer. Since the processes occurring during the interaction of cluster ions of different masses with the surface differ radically [123], many experimental and technological problems require separating a narrow range of masses from the original spectrum. Below, we discuss the methods used to this end.

2.4 Mass separation of cluster ions

One of the simplest ways to filter cluster ions by mass is the retarding potential method, already described in Section 2.2. This method is quite simple and can be used both to filter cluster ions by mass and to determine their mass spectrum. However, it fails to enable separation of a specific range from the initial mass distribution of clusters, since the repulsive electrode reflects only light ions without affecting heavy particles.

Mass separation of a beam of cluster ions is often carried out by means of their deflection in a static magnetic field [124], which can be created by a permanent or electric magnet. If the field induction is equal to B, the length of the region occupied by the field is L_1, and the distance from the magnet to the target is L_2, then a particle of mass M_N deviates in the direction perpendicular to the initial trajectory by a distance

$$y = R - \sqrt{R^2 - L_1^2} + \frac{L_1 L_2}{\sqrt{R^2 - L_1^2}}, \qquad (19)$$

where $R = (1/B)\sqrt{2M_N U_{\mathrm{acc}}/Ze}$ is the radius of the ion trajectory in the magnetic field region. If the target is fixed in a certain position relative to the magnet, only clusters whose masses lie in the required range hit this target. To achieve sufficient mass resolution corresponding to cluster sizes of several thousand atoms, fairly high values of magnetic field induction are required. On the other hand, it is possible to use magnets with low fields in the mode of cutoff of atomic and light cluster ions, i.e., when all clusters whose mass is larger than a threshold value are weakly deviated and are considered to arrive at the same target region [46].

A beam can be filtered in crossed electric and magnetic fields, i.e., the fields oriented perpendicular or almost perpendicular to each other and to the axis of the optical column. Such a mass separator was created by Wilhelm Wien back in 1898 and was named after him (it is also sometimes called an $\mathbf{E} \times \mathbf{B}$ filter or velocity filter). Without deflection, only those particles pass through the Wien filter and the separating diaphragm at the exit of its flight space, the speed of which coincides with the value $v_0 = E/B$, where E is the electric field strength and B is the magnetic induction. Wien filters are usually equipped with permanent magnets with a fixed value of B, and the mass of charged particles (more precisely, the mass-to-charge ratio M/Z) that pass through the filter is controlled by changing the electric field strength E, i.e., the potential difference applied to the electric filter plates. The mass-spectral resolution depends on the mass, velocity, spread of velocities and entry angles of the separated particles, strength of the electric and magnetic fields, and width of the input and output slits of the filter diaphragms along the dispersion axis. The theoretical basis, design, and operating principles of the Wien filter are discussed in detail in [125, 126].

To achieve sufficient mass resolution, well-focused ion beams and narrow input and output apertures are required. Otherwise, a setup similar to the Wien filter can be used in the mode of cutoff of monomers and light clusters (due to their lateral deflection in a magnetic field) and the flow of neutral particles moving together with the flow of cluster ions (due to the deflection of the charged fraction in the required direction in the electric field).

The method to separate clusters by mass based on the already described time-of-flight technique consists in installing a second pair of deflecting plates at the end of the drift space that only open for the time period when ions of the required mass from the pulse generated by the first plates fly between them [127]. Although this method provides a fairly narrow ion mass distribution ($N/\Delta N \sim 12$ at $N = 2000$ argon atoms and $U_{\mathrm{acc}} = 5$ kV), the transmission factor of this system is very low and amounts to several percent, because after passing through the system the ion beam is a pulsed one. This significantly increases the duration of the experiment. In addition, to achieve the specified resolution, the time-of-flight filtration system must have sufficiently large dimensions (most often, more than 50 cm).

A radio-frequency filter developed by Yamada's group [128] has a similar design, but much smaller dimensions (about 20 cm). It also consists of two consecutive pairs of plates (Fig. 15). A sinusoidal voltage is applied to pairs of plates, and the phase of the voltage on the second pair is shifted by a certain amount. The operating principle of the device is based on the fact that, after passing through the first pair of plates, some of the ions continue to move along the axis of the system, but with some displacement from the axis. If these ions approach the second pair of plates in antiphase voltage, the electric field acting between the plates of the second pair returns them to the axis. Since the time during which the ions stay between the plates of each pair and in the gap between the pairs of plates depends on their velocity, which, in turn, depends on the M/Z ratio, it is possible to carry out the mass selection of ions by choosing the frequency and phase shift of the voltages. The resolution of the system $R_{\mathrm{m}} = M/\Delta M$ is about 2, where ΔM is the range of ion masses transmitted by the analyzer at a level of 50% of the signal intensity.

A further extension of this technique is the recently developed mass separator with rotating electric fields, which makes it possible to obtain an ion beam in a continuous mode and with a high resolution independent from the ion mass (for the design described in [129], the resolution is 86). In such a system, the ion beam passes successively through two regions, in each of which an electric field perpendicular to the axis is created. The intensity vector of these fields rotates with the same frequency, but in antiphase. Passing through the first region, the ions deviate from the axis of the system under the

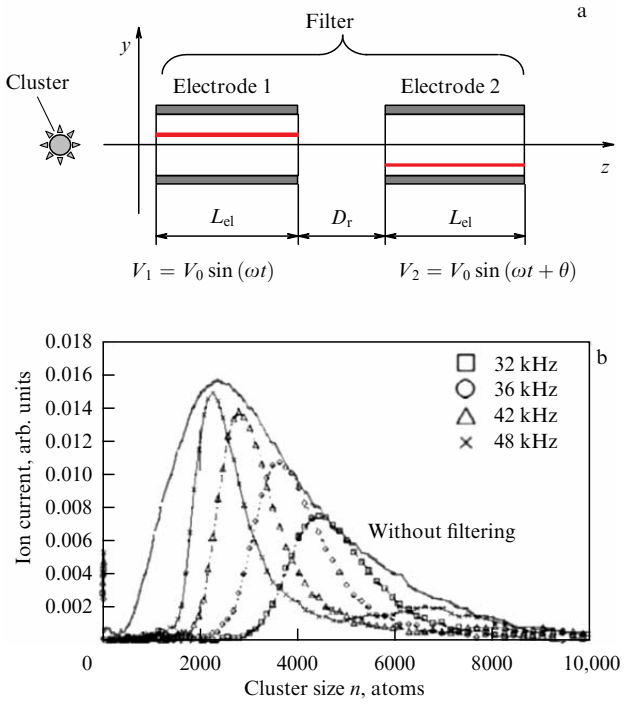

Figure 15. Radio-frequency filter and mass spectra of a beam of cluster ions after passing through such a filter [128]. L_{el} is the length of the plates and D_r is the length of the gap between pairs of plates.

action of an electric field, and in the second region they return to the axis. The mass of ions arriving at the exit diaphragm of the system without velocity components perpendicular to the axis is determined by the rotation frequency of the fields [130].

A pulsed system [131], which is based on a rotation of the ion flow by 90° and is used to separate the primary ion beam in secondary ion mass spectrometry (SIMS), was applied in [132, 133]. In the most recent work, the mass resolution was more than 50.

It should be noted once again that, in all the described methods of ion filtration, separation occurs not by the mass of the ion as such but by the mass-to-charge ratio. As applied to cluster ions, this is a serious problem, since, even with an argon cluster size of more than a hundred atoms, the probability of the existence of doubly charged clusters is nonzero, and with a size of more than 230 atoms, triple-charged ions emerge. Thus, depending on the ionization conditions, a beam of cluster ions with an average size of several thousand atoms can contain a fraction of multiply charged ions. After passing through the accelerating potential difference, such ions have a kinetic energy twice (or more) as large as that of singly charged ions. The effects arising from the interaction of such high-energy ions with a surface can differ significantly from the case of singly charged ions. Since such ions are not removed from the beam by the systems described above, the processes associated with them can become dominant [134], which should be taken into account in interpreting the experimental results.

Nevertheless, study [111] describes the principle of determining the average charge, average energy, and average mass of cluster ions in a beam. It is based on the independent measurement of the average energy-to-charge ratio $(E/q)_{av}$ using an electrostatic energy analyzer, the average velocity v_{av} using a time-of-flight system, and the average charge q_{av}. The average charge is found by determining the flow of particles using a luminescent counter and the current transported by these particles to a Faraday cup. Assuming these quantities are uncorrelated, the average energy can be calculated as $E_{av} = q_{av}(E/q)_{av}$, and the average mass, as $M_{av} = 2E_{av}/(v_{av})^2$. Thus, it was shown that, under the conditions described in this article, Ar cluster ions with an average mass corresponding to 10,400 argon atoms, accelerated by a voltage of 30 kV, have an average charge of 3.2 and an average energy of 64.5 keV. It is of interest that, in these experiments, the average energy per charge was always significantly lower than 30 keV. This can be explained by the fragmentation of cluster ions due to Coulomb destruction and interaction with the residual gas.

2.5 Designs of cluster ion sources

We now present some examples of sources of gas cluster ions currently in operation which are used to solve various technological and scientific problems. nAccel 100, a gas cluster ion accelerator developed by Exogenesis (USA) (Fig. 16) [135], can be considered as an example of an industrial facility designed to modify the surface of large substrates.

The accelerator consists of three vacuum chambers: the nozzle chamber, the ionizer chamber, and the working chamber. In the first chamber, neutral clusters are formed when the working gas expands through the nozzle. The gas flow is 50–500 sccm. Having passed through the skimmer, the clusters enter the next vacuum chamber, where they are ionized and accelerated by a potential of 10–50 kV. A distinguishing feature of the system is the option to operate it in the mode that generates an accelerated neutral atomic beam (ANAB). To this end, deflecting plates are installed at some distance after the accelerating electrode. By applying a constant voltage to the deflecting plates, it is possible to completely remove charged clusters from the beam. In this case, neutral atoms formed during partial or complete destruction of clusters due to interaction with atoms of residual gases pass through the deflecting plates without changing the trajectory. The kinetic energy of such atoms approximately corresponds to the energy per atom in the cluster ion, i.e., is several ten eV. A calibrated system consisting of a calorimeter and a pressure sensor is used to measure the flow of matter carried by cluster ions or neutral atoms and their average energy. The average energy in a beam of accelerated neutral atoms as a function of the acceleration voltage of cluster ions is shown in Fig. 17. Unfortunately, the parameters of the nozzles used are not disclosed.

The use of cluster ions makes it possible to attain significant values ($10^{14} - 10^{16}$ atom s^{-1}) of fluxes of neutral

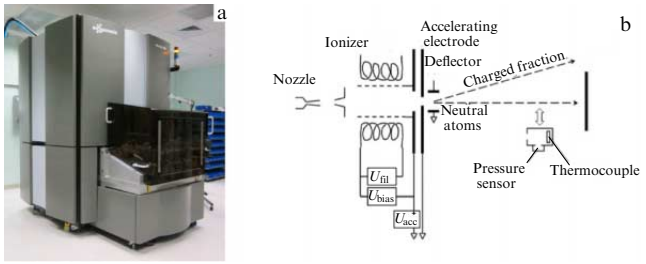

Figure 16. External view (a) [135] and circuit diagram (b) [136] of the nAccel 100 accelerator. Diagram shows the power source: U_{fil} is the cathode filament, U_{bias} is the voltage between the cathode and the anode, and U_{acc} is the accelerating voltage.

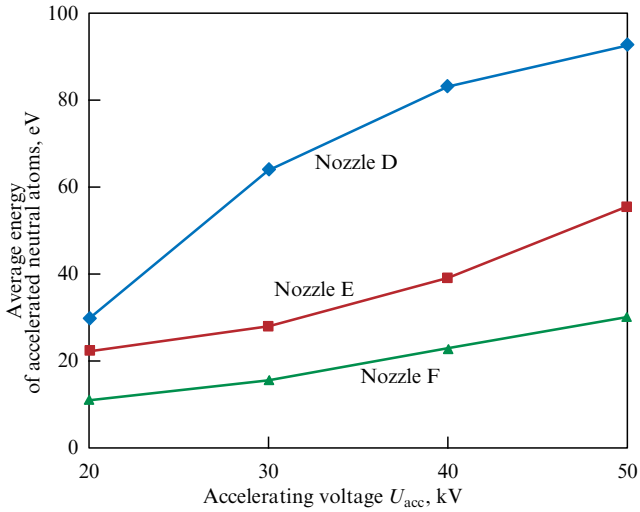

Figure 17. Average energy of accelerated neutral atoms at various acceleration voltages of cluster ions [136].

atoms accelerated to energies of 10–100 eV. Owing to this, it is possible to modify the topography of the surface and its biocompatibility properties and implant substances at ultra-shallow depths without creating defective layers in the bulk of the substance for both conductive and dielectric samples [136, 137]. The working chamber of the system is equipped with a manipulator that allows processing substrates with dimensions up to 310×310 mm in the mode of mechanical scanning of the sample.

As a disadvantage of the system, the absence of mass separation of charged particles can be noted. This implies that, along with cluster ions, atomic ions accelerated to the same energies can also hit the sample.

Sources of cluster ions [109, 138, 139] (Fig. 18) used in analytical techniques, such as SIMS and XPS, are used for defect-free surface cleaning, for layer-by-layer etching in the process of depth profiling, and as analytical probes. These processes are discussed in more detail in Section 3.2.

Such sources must provide a high lateral resolution, so the beam of cluster ions can be focused to a diameter of several microns or less. Mass separation is carried out using a Wien filter. Cluster sizes vary from a few to more than 10^4 atoms per cluster at an energy of 10–40 keV, and the cluster ion currents after mass separation are several ten nA. Given the small diameter of the ion beam, such a current provides an ion current density sufficient for efficient local etching of the sample material. The formation of a low-current beam of cluster ions does not require intensive pumping of the source chamber, so turbomolecular pumps with a pumping rate of 100–300 l s^{-1} are used in the vacuum system of sources.

Accelerators used in laboratory research are described, for example, in [28, 46, 141, 142], and an image is shown in Fig. 19. Such accelerators make it possible to quickly modify the system (replace ionization and mass separation systems or install additional manipulators or analyzers), depending on the problem being explored. In particular, study [142] describes a cluster ion accelerator developed at Lomonosov Moscow State University. To reduce the load on the pumping system of the nozzle chamber, a pulsed mode of supply of working gas to the nozzle is used, which has a critical section of 130 μm at an opening angle of 11°. The ionizer was developed on the basis of indirectly heated cathodes and a mesh

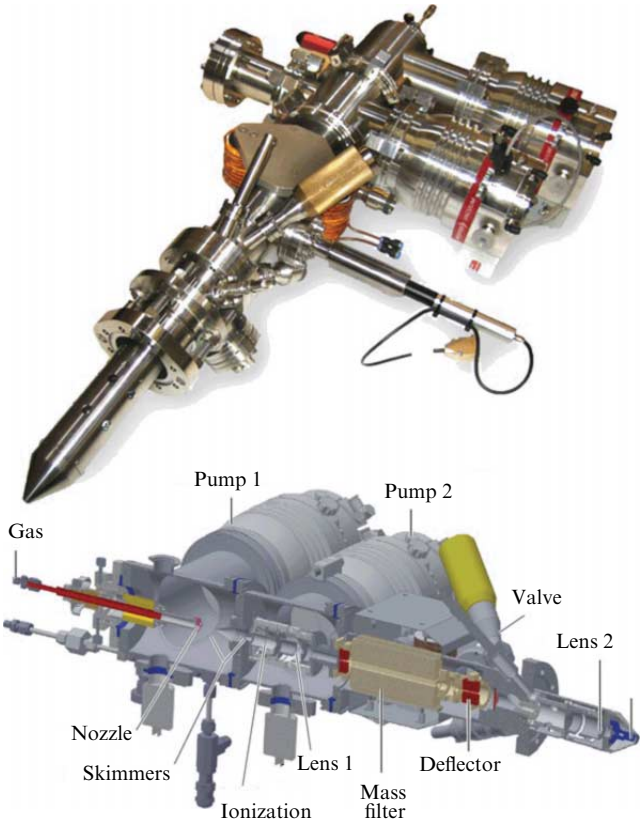

Figure 18. Source of cluster ions, Ionoptica GCIB 40 [139, 140].

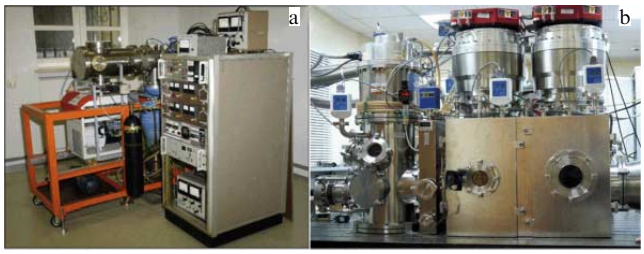

Figure 19. (a) External view of the laboratory accelerator of gas cluster ions developed at Moscow State University [46], (b) external view of the CLIUS experimental device (Department of Applied Physics, Faculty of Physics, Novosibirsk State University).

cylindrical anode (Fig. 12b). After the cluster ions are accelerated to energies of 1–15 keV, they are mass-separated in a static magnetic field and focused on the target. The time-of-flight technique is used to measure the size distribution of cluster ions. The target is mounted on a manipulator with three degrees of freedom or on a manipulator of the system that longitudinally moves samples, which makes it possible to irradiate samples of complex shape or several samples in succession.

3. Applications of gas-dynamic sources of cluster ions

The characteristics of interaction of accelerated cluster ions with matter drastically differ from those of atomic ions with the same energy. This is essentially determined by the specific feature of the release of energy in collisions with the surface. The kinetic energy of a cluster is distributed among the atoms

of which it consists: for example, if Ar_{1000} clusters accelerated to an energy of 10 keV are used, the kinetic energy of each atom (specific energy) is only 10 eV. Such atoms are decelerated in the uppermost layers of the target, and virtually all the energy of the cluster is released in a region about 1 nm deep. However, atomic argon ions with an energy of 10 keV penetrate into the substance to a depth of the order of 10 nm (for example, the average projective range of argon in silicon is 15 nm [143]), dissipating kinetic energy along the entire track. On the other hand, it is incorrect to compare atomic ions with cluster atoms with the same energy, since, in the latter case, a larger number of cluster atoms concurrently interact with a local surface area. For example, the threshold of sputtering by cluster ions turns out to be significantly lower than that for atomic ions due to collective interaction. For instance, the threshold of sputtering copper by Ar_{3000} clusters was less than 3 eV per atom [144], while the threshold for sputtering by atomic argon was about 30 eV [145].

A detailed analysis of the physical processes that occur in the collision of an accelerated cluster with a matter is beyond the scope of this review. Nevertheless, we briefly consider the processes and regularities that are the most important for a particular area of application of the sources of gas cluster ions.

3.1 Modification of surface properties by beams of gas cluster ions

3.1.1 High-precision polishing of a surface. One of the most common applications of cluster ions is the smoothing of a surface profile under normal incidence of an ion beam. In addition to the possibility of obtaining surfaces with a residual roughness at a level of tenths of a nanometer, the advantage of this method of smoothing compared with alternative ones (abrasive or electrochemical polishing or magnetorheological or chemical and mechanical processing) is that chemical agents specific to each particular material are not needed and the target is not contaminated with impurities. Currently, the following physical mechanisms are generally believed to be responsible for smoothing.

One of the specific features of sputtering by cluster ions is the presence of the so-called lateral angular distribution of the sputtered substance. It is known that, in the case of sputtering by atomic ions with energies of the order of keV, the angular distribution of the knocked-out atoms is close to the cosine, i.e., the larger part of the differential yield $d^2Y/d\Omega^2$ is directed along the normal to the surface. In the case of cluster ions, a significant part of the knocked-out atoms is directed at large angles to the normal line, i.e., along the surface [146, 147]. As a result, if a cluster gets into a depression of the surface relief, the yield of the sputtered atoms is partly blocked by depression walls. Therefore, the efficiency of sputtering of depressions turns out to be significantly lower than that of protrusions, which has been clearly shown using computer simulation [148]. Moreover, there is a high probability of secondary deposition of the laterally sputtered atoms and their subsequent diffusion into the depression area, which also results in smoothing of the roughness [149].

An important issue in assessing the efficiency of smoothing is the method used to assess roughness. Most frequently, to measure the topography of smooth surfaces processed using cluster ions, atomic force microscopy (AFM) is applied, which provides a fairly high resolution, both over the height and along the surface. In this case, roughness can be numerically characterized by average R_a or root-mean square (RMS) R_q values, which are, respectively, determined by the following formulas:

$$R_a = \frac{1}{n}\sum_{i=1}^{n}|h_i|\,, \quad R_q = \frac{1}{n}\sqrt{\sum_{i=1}^{n}h_i^2}\,, \tag{20}$$

for n measurements of height h_i with respect to the mean line.

For many applications associated, for example, with the manufacture of reflective surfaces, it is necessary to know not only the value of the roughness but also its character, i.e., lateral scales, the presence of distinguished directions, etc. In this case, the power spectral density function (PSD) or the two-dimensional Fourier transform is used. In addition, the flicker-noise spectroscopy approach was developed in [150] to characterize the relief features of smooth surfaces. Finally, it is possible to separate the relief into components of different natures and to analyze separately the effect of ion irradiation on each of these components. As an example, we consider the surface of an optical glass-ceramic (two-phase material containing crystalline inclusions in the amorphous phase [151]). The relief of the polished glass-ceramic surface is formed by protrusions corresponding to crystallite outcrops, scratches that appear as a result of abrasive or chemical-mechanical polishing, and residual chaotic components. The super-smooth surface of glass-ceramic glass polished by a beam of cluster ions by separating the components of the relief was studied in [152].

In describing the roughness, it is of importance, first, to indicate the size of the scanning area over which the values of R_a or R_q were calculated, since, depending on the size of the area, roughness with different spatial scales can be included in the frame. In addition, one of the features of AFM image processing is the subtraction of the underlying surface of the n-th order, which can also result in incorrect interpretation of the measurement results if frame size is chosen incorrectly. Second, it is necessary to make sure that the obtained images reliably characterize the relief of the entire surface, i.e., adding new images to the array of processed data does not change the obtained roughness values. For example, if solitary protrusions are randomly distributed over the surface, the measured characteristics of the surface strongly depend on the number of protrusions in the frame [153].

The beginning of active research on the effect of surface smoothing by cluster ions dates back to the mid-1990s [154, 155]; over the past two decades, the possibility of using cluster ions to smooth the surface of a wide range of various materials has been demonstrated. Figure 20 shows the evolution of the relief on the surface of a copper film under the effect of irradiation with 20-keV Ar_{2000} cluster ions [156]. The average roughness decreased from 6 nm to 1–1.3 nm upon reaching a dose of 3×10^{15} ion cm^{-2}. The thickness of the layer removed by the clusters was about 25 nm, and this value is close to the height difference on the initial surface. It is emphasized in [156] that the height difference between various crystallites is not visible on the irradiated surface. Nevertheless, this observation does not imply that the rate of sputtering of single crystals by cluster ions does not depend at all on the crystallographic direction. For example, for a NiPd alloy irradiated with 20-keV Ar_{2500} clusters, when a dose of 10^{17} ions cm^{-2} was reached, the height difference between crystallites was about 10 nm [157].

In addition, it should be emphasized that, in many studies on the ion smoothing of metals, films rather than bulk targets were used. This implies that, in addition to the process of

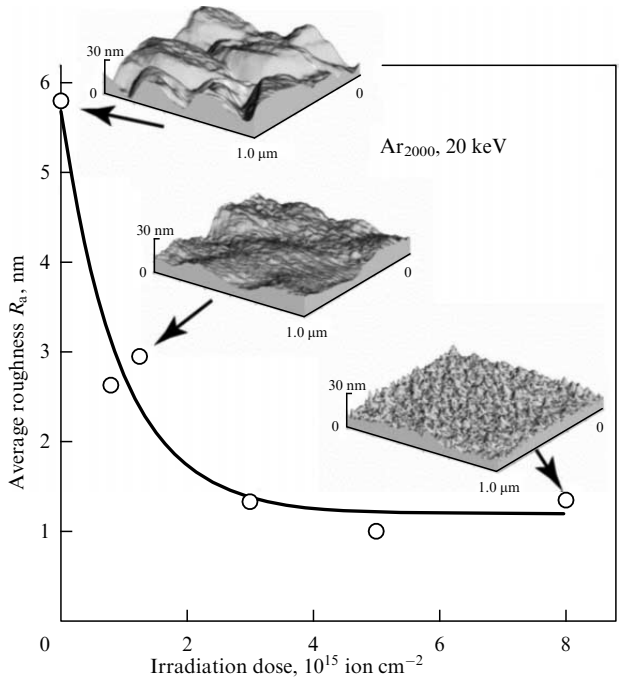

Figure 20. Evolution of the surface relief of a polycrystalline copper film upon irradiation with 20-keV Ar_{2000} cluster ions [156].

surface smoothing by cluster ions per se, the results obtained can also reflect effects related to the thickness and intrinsic structure of the films. The modification of thin (less than 30 nm) silver films used as plasmonic waveguides is described in [158, 159]. The problem of obtaining such films on dielectric substrates is related to the island mechanism of their growth. As a result, the film features a polycrystalline structure and significant roughness, and, at a thickness of less than 10 nm, it is not even continuous, i.e., it loses conductive properties. This, in turn, results in a significant deterioration of the plasmonic qualities of the film.

Irradiation of a 70-nm-thick Ag film with 20-keV nitrogen cluster ions consisting of several thousand atoms led to a decrease in the root-mean-square roughness from 5 nm to approximately 1 nm at a dose of 10^{16} ion cm^{-2}. The residual film thickness in this case was 25 nm. In addition, under irradiation with clusters, the average crystallite size increased by a factor of three, while, when the film was etched to a thickness of 5.8 nm, it still remained conductive. Bettering the surface roughness and bulk structure of the film via irradiation with cluster ions led to an enhancement of the electrical and optical properties of the structures, an increase in the propagation length of waves in waveguides, and an improvement in the characteristics of optical-range plasmonic filters.

In addition to smoothing roughness in the nano- and micrometer ranges of lateral sizes [160], corrective etching with cluster ions can be used to eliminate roughness with lateral sizes on the order of centimeters. Indeed, knowing the profile of the beam ion current density and the target etching rate, a program can be set to move the treated surface relative to the ion beam for high-precision correction of the shape of this surface [161, 162]. In the case of cluster ions, this option has been demonstrated, for example, in [121, 122] for the planarization of eight-inch silicon and silicon-on-insulator wafers. To increase the etching rate, chemically active 30-keV Ar/SF_6 clusters were used. The thickness of the removed layer reached 3 μm at a dose of 10^{16} ion cm^{-2}. The height difference along the entire surface of the plate was reduced from 540 to 77 nm.

Considerable attention is drawn to the possibility of polishing the surface of superhard materials such as diamond or silicon carbide. For example, diamond membranes produced by the CVD (chemical vapor deposition) technique, which are intended for X-ray lithography, have been polished [163]. Beams of Ar and O_2 clusters with an energy of 20 keV and a size of 2000 atoms per cluster were used to this end. Under these conditions, the sputtering yield of oxygen clusters is approximately an order of magnitude greater than that of argon clusters due to chemical sputtering. Irradiation with chemically active oxygen clusters did not lead to surface smoothing. Irradiation with argon clusters at a dose of 10^{17} ions cm^{-2} enabled a reduction in the average roughness from 130 to 60 nm; however, this treatment resulted in the emergence of a graphitized layer on the surface, which deteriorated the optical characteristics of the membrane. This layer was removed by additional irradiation with oxygen clusters at a dose of 10^{15} ion cm^{-2}. It should be noted that the emergence of the damaged layer was due to the presence in the beam of a small fraction of atomic ions transmitted by the employed mass separation system.

Rutherford back scattering (RBS) in the channeling mode [164] and Raman light scattering [165] were used to show that the complete removal of atomic ions from a beam leads to a significant decrease in defectiveness on the processed surface. In the latter study, mechanically polished single crystals of diamond and silicon carbide were smoothed using argon clusters with an average size of 1000 atoms per cluster and an energy of 10 keV. At an irradiation dose of 5×10^{16} ions cm^{-2}, the root-mean-square roughness was reduced by approximately a factor of two from the initial values of about 3 nm. In addition, in the case of silicon carbide, the diamond background (scratches that emerged as a result of abrasive polishing) was completely removed.

In [166], on the contrary, polycrystalline samples of silicon carbide irradiated with argon clusters showed an increase in the average roughness, which was reduced as a result of irradiation with oxygen clusters. In the case of polycrystalline yttrium aluminum garnet (YAG), the scratches remaining after mechanical polishing were completely removed by irradiation with 30-keV argon clusters at a dose of 10^{17} ions cm^{-2}. As the dose was increased to 10^{18} ion cm^{-2}, a further decrease in roughness to subnanometer values was observed. Even at such a significant dose, the difference in the heights of adjacent crystallites, which is due to the dependence of the etching rate on their orientation, was only 2.7 nm. When trying to remove scratches using chemical and mechanical polishing, the average roughness increased due to the manifestation of the crystallite structure.

Ytterbium-doped yttrium-aluminum garnet (Yb:YAG) is a promising material used as an active medium in high-power laser systems. One of the factors that limit the perfection of such systems is the quality of the interface between the active medium and its optical coating. Processing such a medium, carried out in the nanotexturing mode (using 30-keV argon cluster ions) and in the polishing mode (using successive irradiation with argon clusters and accelerated neutral atoms), resulted in surface cleaning and an increase in the optical power threshold of the crystal by a factor of 1.5 to 2 [137]. After applying the optical coating, the power threshold for nanostructured crystals turned out to be higher than that

for polished ones. This is related to an increase in the quality of the interface between the coating and the substrate.

Cleaning and additional polishing of the ultrasmooth surface of potassium titanyl phosphate, a nonlinear optical crystal also used in high-power laser systems, was carried out in [167], but the optical characteristics of the processed crystals were not studied in this work. It should be noted that, in addition to the interface layers per se, the characteristics of optical crystals are also affected by the presence of defects in deeper regions, where absorption and scattering of radiation can occur, leading to the destruction of the crystal [168]. These defects can emerge in regions up to hundreds of nanometers deep as a result of crystal polishing by conventional methods, and etching with cluster ions would make it possible to remove defective regions [169]. However, to date, such work has not been carried out.

As already mentioned, irradiation with cluster ions of sufficiently high energies can be accompanied by amorphization of the surface under processing. The mechanisms that govern the formation of amorphous layers have been explored in numerous experiments [170, 171] and numerical simulations [172]. However, a significant proportion of experimental studies is based on the results obtained by indirect methods: ellipsometry [173] or the RBS method in determining the broadening of a subsurface thin layer [174]. Direct determination of the thickness of the damaged layer on the silicon surface using medium energy ion scattering (MEIS) yielded values of approximately 10 nm for an argon cluster energy of 20 keV, 6.4 nm for an energy of 10 keV, and 4.2 nm for an energy of 5 keV [175]. Irradiation with cluster ions was carried out using a ULVAC-PHI source. The angle of incidence of the clusters was 55° with respect to the normal, and the average size was 2500 atoms per cluster. The fraction of argon implanted into the target was negligible compared to the case of irradiation with atomic argon ions (in the latter case, it was on the order of 5–8%).

It is known that high-temperature recrystallization makes it possible to controllably restore the structure of an amorphized target [176]. For example, the amorphized layer formed upon irradiation of single-crystal silicon with cluster ions of argon and SF_6 was completely removed from the substrate as a result of annealing in a hydrogen atmosphere at a temperature of 1473 K due to recrystallization directed away from the substrate [177]. The layer thickness depended on the energy and material of the clusters, and at an energy of 30 keV it was about 30 nm and 5 nm for Ar (physical or ballistic sputtering) and SF_6 (chemical or reactive sputtering) clusters, respectively. Unfortunately, the sizes of the clusters are not given in the paper. It is of interest that, in the process of irradiation, a characteristic relief was first formed, as a result of which the surface roughness on small lateral scales increased, but, upon annealing, this roughness was smoothed to the atomic level of smoothness.

On the other hand, in processing materials with an initially amorphous structure, it is desirable that the processing not lead to crystallization. Although the energy released in such systems during a collision of a cluster with a substance can cause crystallization, if the cooling time of the excited region is less than the critical one, the material remains amorphous. For example, in the case of $Ni_{52.5}Nb_{10}Zr_{15}Ti_{15}Pt_{7.5}$ metallic glass, smoothing was demonstrated from an RMS roughness of 12 nm to 1.1 nm (at a dose of 0.5×10^{16} cm^{-2}) and 0.7 nm (at a dose of 2×10^{16} cm^{-2}) in the absence of crystallization [178]. The size of argon clusters was about 3000 atoms at an energy of 30 keV.

The smoothness of and absence of defects on the surface are the basic requirements for state-of-the-art multilayer magnetic and superconducting structures. Since the topography of thin films most often reproduces that of the surface on which these films were deposited [179], polishing both the substrate itself and its individual layers is generally suitable for improving the quality of the structure. An example is the structure of magnetoresistive random access memory (MRAM). In study [180], a Ru sublayer 5–50 nm thick was irradiated with 5-keV nitrogen clusters; a correlation was found between the roughness of the sublayer, the roughness of a thin film deposited on it, and the quality of the formed magnetic tunnel junction. The evolution of the film surface topography is shown in Fig. 21.

To reduce the imperfection introduced into the upper layers of the target by cluster ions, irradiation at grazing angles can be used. In this case, as simulation by the molecular dynamics method shows, clusters remove small protrusions more efficiently [181], virtually without creating defects due to the small value of the normal component of the momentum. Although in a certain range of angles a relief can be formed instead of smoothing the surface (see Section 3.1.2), at sufficiently large angles of incidence (about 80° with respect to the normal) and using sample rotation during irradiation, smoothing of magnetic materials has been demonstrated (NiFe, PtMn) up to an average roughness of 1.2 nm with a defect layer thickness of less than 1.5 nm [182]. In this case, in contrast to polishing with conventional beams of atomic ions, the stress profile in the film remained virtually unchanged. An improvement in the quality of the surface of films of high-temperature YBCO superconductors was shown, for example, in [183, 184].

Smoothing by clusters under grazing incidence offers a method for polishing surfaces, the possibility of normal irradiation of which is limited, for example, the waveguide walls and the side surfaces of resonant structures of backward wave tubes. Polishing of the side surfaces of sub-micrometer structures etched in silicon was shown in [185], where a method to enhance the quality of photonic structures is discussed. Polishing of vertical gold mirrors used in microelectromechanical systems (MEMS) was carried out in [186]. One of the promising materials of modern technology is $LiNbO_3$, which features ferroelectric properties [187, 188]. Although studies of the regularities of the formation of a layer with an altered composition and structure on its surface as a result of bombardment by clusters began relatively recently [189], waveguides with low losses, promising for applications in integrated optical devices, have already been obtained using cluster polishing of side surfaces [190].

The study of the evolution of micro- and nanostructures under irradiation with cluster ions is of interest from the point of view of both understanding the mechanisms of sputtering and the formation of surface morphology and the controlled modification of these structures. The efficiency of smoothing irregularities by an ion beam apparently depends on the lateral dimensions of these irregularities. Consequently, it is possible to select a mode that results in the selective removal of irregularities with given lateral dimensions. Such an approach can be used to 'smooth out' small-scale roughness on the grooves of echelette diffraction gratings with an atomic ion beam while preserving the grooves themselves [191], which leads to an enhancement of the diffraction efficiency of the gratings. On the other hand, in using bombardment with cluster ions with certain doses and angles of incidence, it

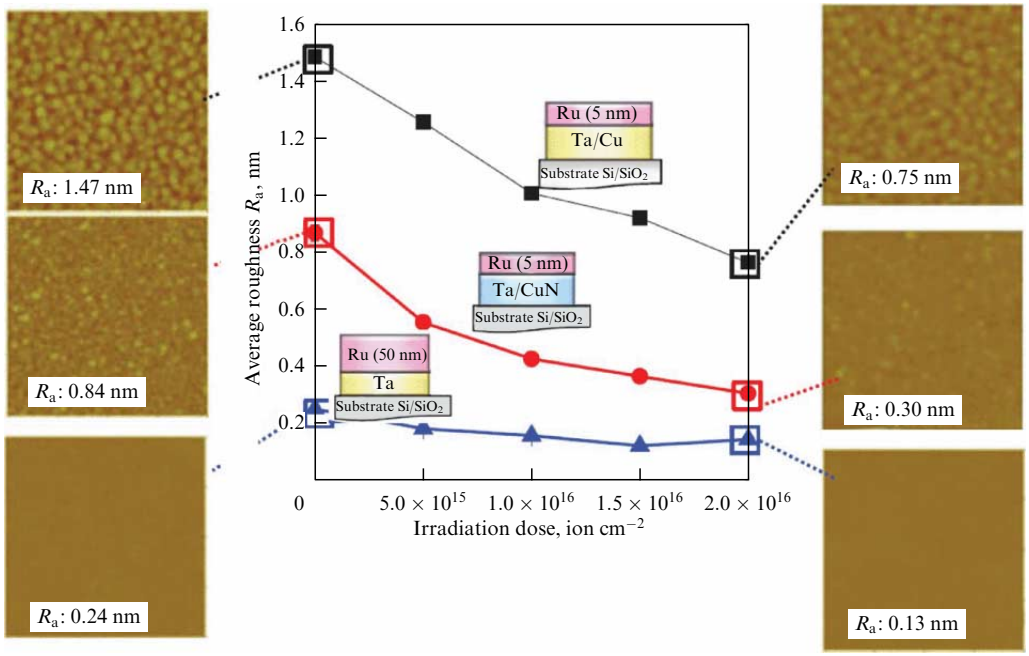

Figure 21. Average roughness of thin-film structures as a function of a dose of irradiation by 5-keV nitrogen clusters [180].

is possible to correct the shape of the grooves themselves, set angles of inclination to their faces (blaze angles), etc. [192].

In addition to surface-structured materials, the use of metamaterials, for example, based on layers of porous silicon with alternating porosity, is widely discussed in optical research [193]. The observation of nonlinear optical effects in such structures is hindered by the strong scattering of light by inhomogeneous structures that emerge on the cleavages of the structures. Irradiation with cluster ions leads to a significant increase in the homogeneity of the cleavage surface and, as a consequence, to an increase in the specular reflection coefficient, i.e., to a decrease in light scattering in a wide range of wavelengths [194].

Technologies related to the development of structured data carriers (BPM — Bit-Patterned Media) are based on the use of an array of magnetic cells to record information. However, to achieve a sufficient speed of movement of the reading head, the surface of such a carrier must be perfectly smooth. To obtain a smooth surface, a film of nonmagnetic material is deposited on a structured surface. This film can be smoothed during deposition (assisting with cluster ions in the processes of deposition of amorphous carbon from a fullerene flow [195]) or after deposition (filling grooves in carbon films [196], films of Cr, Ta, SiO_2 [197]).

Another technology area in which high surface quality is required is the development of linear particle accelerators. The values of electric fields in the cavities of modern accelerating structures can reach tens of MV cm^{-1}. One of the problems that limits the strength of the electric field, and hence the rate of energy gain, is dark currents and single RF breakdowns. Although the description of the mechanisms of these phenomena can hardly be called exhaustive at present, it is clear that they are largely related to the roughness and cleanliness of the surface of the cells of the accelerating structures. A series of theoretical and experimental studies on smoothing of the materials, including superconducting ones, which are used in such structures was carried out with the participation of Insepov (see Refs [198–200] and references therein). Later, smoothing of the surface of real cells of accelerating structures made of copper was demonstrated [201]. However, we are unaware of studies of the characteristics of accelerators, in the manufacture of which the technology of cluster polishing was used.

Summarizing this section, we note that the results of using cluster ions for surface polishing described in publications, albeit numerous, are fragmentary and unsystematic. Irradiation doses (depending on the material being processed and the initial state of the surface) in the described experiments varied over a wide range ($10^{15} - 10^{18}$ ion cm^{-2}); however, most of the studies only explored a narrow range of doses, most frequently for invariable energies and the same size and type of cluster ions. There is currently no predictive, albeit empirical, model for the evolution of the relief under irradiation by clusters.

Regarding an enhancement of the efficiency of surface polishing, stepwise processing is of interest, i.e., changes in characteristics, for example, specific energy or type of cluster ions during processing. The approach is based on the observation that clusters with a higher specific energy are more efficient in etching and removing the initial relief; however, they can create large craters on the surface, upon overlapping of which a residual relief is formed [202, 203]. Irradiation with such clusters also results in the formation of a significant number of defects in near-surface layers. To eliminate the residual relief and defective layers, it is possible to use clusters with lower values of specific energy or chemically active low energy clusters [204, 205]. Study [206] showed stepwise polishing of an optical glass-ceramic by means of sequential use of beams of accelerated cluster ions and neutral atoms.

Along with the specific energy, which can be varied by choosing the total energy or the size of the clusters, the type (elemental or chemical composition) of cluster is an important characteristic that determines the features of the interaction with the surface [207]. For polishing, argon or nitrogen clusters are usually used, or oxygen or SF_6 clusters

which enable reactive etching. However, direct comparisons of the efficiency of polishing using inert clusters of various compositions are virtually unavailable. It has been shown that xenon clusters, which have the same energy as and a mass distribution close to that of argon clusters, make it possible to obtain the same smoothness of the silicon carbide surface at significantly lower irradiation doses [208]. Although xenon is much more expensive than argon, due to the higher efficiency of condensation, the formation of Xe clusters requires a smaller gas flow through the nozzle.

3.1.2 Formation of an ordered relief. Methods to form nanorelief widely used today, which are based on photo-, electronic, or nanoimprint lithography and direct structuring by focused ion beams, require masks or templates, or they are very limited in area and are time consuming. Therefore, the possibility of forming a nanorelief due to self-organization processes under the action of ion beams seems a promising option [209]. In the case of cluster ions, along with the possibility of smoothing the surface relief under normal incidence of cluster ions, tilted incidence can be used to form an ordered wavelike relief (ripples) on the surface [210]. Some patterns of formation and examples of the application of such wavelike structures are given in review [211], and their typical form is shown in Fig. 22.

The formation of a relief under the effect of a flow of atomic ions is well known, and approaches have been developed to describe the mechanisms of its emergence [212, 213]. In the case of cluster ions, the reasons such a relief appears are not entirely clear; as a possible reason, the dependences of the sputtering coefficient and the transfer of the target material along the surface on the incidence angle are considered [214].

We now consider some patterns of ripple formation. A wavelike relief perpendicular to the plane of incidence of the ion beam is formed in a certain range of angles, approximately $30° - 70°$ from normal. At large angles, the waves are reoriented in such a way that the wave vector becomes perpendicular to the beam incidence plane [215]. Published data on such a regime are fairly scant, and it is possible that at large angles of incidence elongated traces of individual collisions of clusters rather than an ordered relief are observed. With an increase in the radiation dose, the wavelength and amplitude of the waves increase. For example, for SiO_2 irradiated with argon clusters with an average size of about 3000 atoms per cluster and an energy of 30 keV, with an increase in the irradiation dose from 10^{16} to 8×10^{16} ion cm^{-2}, these values increased from 370 to 630 nm and from 70 to 130 nm, respectively [215]. The evolution of the relief as a function of the angle of incidence and irradiation dose for an Si target was examined in [216], and study [217] showed that the nature of the relief is independent of the crystallographic orientation of the Au target. There are indications that, as the energy of cluster ions increases, the wavelength and amplitude of the ripples also increase [218]. Another way to control the relief parameters is to change the temperature of the substrate during the sputtering process. At sufficiently high temperatures, due to the stimulation of surface diffusion, the relief can be smoothed out instead of being formed [219]. At intermediate temperatures, a manifestation of the crystal structure of the samples was observed: ripples were formed only if one of the crystallographic directions of the lattice coincided with the plane of incidence of ions [220].

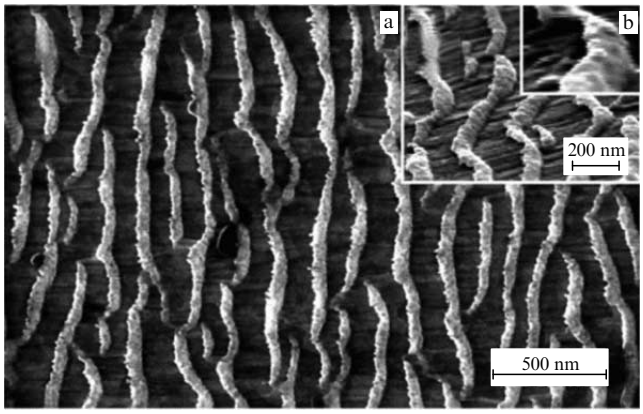

Figure 22. Images of a nanorelief formed on gold upon irradiation with cluster ions at a dose of 4×10^{16} ion cm^{-2} at an incidence angle of 60°. (a) Top view, (b) view at an angle of 70° [211].

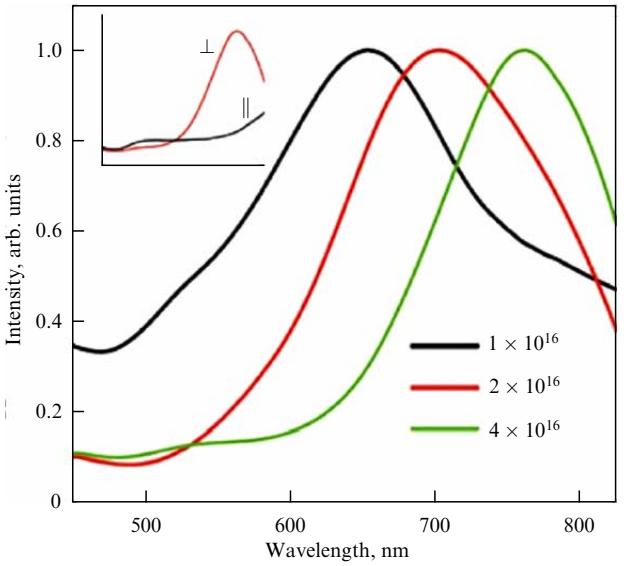

Figure 23. Spectra of diffuse light scattering by a nanostructured gold surface. Inset shows spectra for various polarization orientations relative to the ripple wave vector [221].

Structured metal surfaces attract attention due to the possibility of implementing plasmon resonance in nanostructures and creating plasmon filters, sensors, surface enhanced Raman scattering (SERS) substrates, etc. on their basis. Anisotropic wavelike structures formed under the effect of cluster ions are also sensitive to the direction of light polarization with respect to the wave vector of the structures (Fig. 23). The position of the maxima of plasmon characteristics can be easily controlled by choosing the irradiation parameters, i.e., by changing the amplitude and length of the waves.

If organic molecules are immobilized on the surface of the structure, the dielectric characteristics of the medium change, and the position of the plasmon resonance maximum shifts. Thus, it becomes possible to create sensors sensitive to specific organic and biological molecules (Fig. 24) [222, 223].

If the irradiated substance is a multicomponent one, then, in addition to the formation of the topographic relief per se, areas of different compositions can be formed on the surface. For example, if an InP semiconductor compound is bombarded with atomic argon ions, due to the predominant

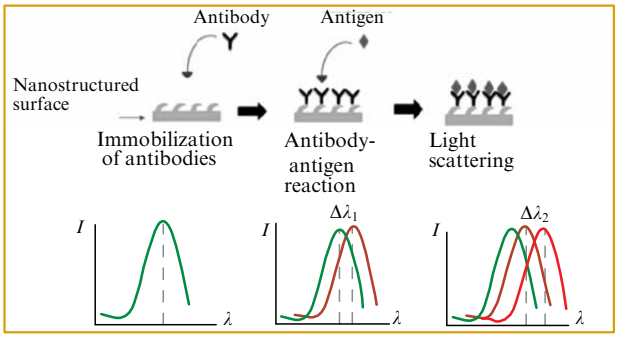

Figure 24. Antibody–antigen reaction (AB–AG) sensor based on a shift of the plasmon resonance maximum in nanostructures [222].

sputtering of phosphorus, the surface is enriched with indium, which, as a result of surface diffusion, can cluster into islands and be used as a mask for further formation of a relief in the form of columns [224, 225]. It was also shown that indium islands are formed during bombardment with cluster ions [226]. A promising direction in using such metal islands on a semiconductor substrate is the creation of SERS substrates, quantum informatics devices, and integrated optical circuits and switches.

Indium phosphide is a compound with a constant ratio of components, due to which, if this ratio is violated because of selective sputtering, phase separation can occur. For solid solutions, i.e., substances that allow a change in the ratio of components over a wide range, the ripples formed during tilted irradiation with cluster ions are also enriched in one of the components of the solution [157], i.e., components can be redistributed over the surface in an ordered way.

3.1.3 Modification of surface chemical properties and stimulation of surface chemical reactions. In addition to altering the surface topography, during bombardment with ions, the chemical composition of the surface and near-surface layers can change due to the introduction (implantation) of cluster material into the target, chemical reactions with substances of the ambient atmosphere or contamination, and removal of target components in the process of sputtering.

Direct connection of plates is currently widely used in microelectronics and microsystem technology. To ensure good contact between the materials to be connected, their surfaces must be very smooth. One of the ways to stimulate the process is surface-activated bonding (SAB) [227]. In the process of activation argon ion bombardment removes adsorbed contaminants and natural oxides from surfaces to form direct bonds between the plates. As an alternative to atomic argon ions, it was proposed to irradiate copper plates with cluster ions [228]. In this case, two irradiation regimes were used: normal incidence of clusters with a dose of 10^{16} ions cm^{-2} and an energy of 20 keV to smooth the initial surface relief, and subsequently tilted (at an angle of 70° with respect to the normal) to remove oxides, i.e., for actual activation. Complete removal at normal incidence would require a high dose of irradiation due to the mixing effect under sputtering. In addition to an enhancement of the strength of joint as opposed to untreated samples and samples treated with atomic Ar ions, a significant decrease in the wetting angle was observed. Unfortunately, the results obtained for the case of irradiation with cluster ions at normal incidence alone, without the second stage of processing, are not presented in [228]. The use of tilted incidence to remove oxide from copper and silicon in the implementation of SAB is also discussed in [229, 230].

Modification of the chemical and energy state of the surface of metals and polymers using ion irradiation is used to improve the complex biomedical properties of materials [231, 232]. Surfaces irradiated by cluster ions or flows of accelerated neutral atoms also exhibit higher biocompatibility [233]. More efficient proliferation of osteoblasts on titanium, polyetheretherketone (PEEK), and other materials is achieved, as is generally believed, due to surface nanotexturing, charge accumulation on the surface, and amorphization of near-surface layers [234–237].

Local temperatures in the region of a collision of a cluster with a surface reaching tens of thousands of degrees [238–240] stimulate chemical reactions in this region. Such reactions can lead to reactive (chemical) sputtering, which has been discussed earlier, or to the formation of chemically modified layers on the surface [241]. The rates of reactive sputtering by cluster ions can be several times higher than those of physical sputtering, and the chemically active substance can be components of the clusters themselves (for example, ethanol [242], acetone [243], SF_6 [244]) or come from the ambient atmosphere [245, 246]. The latter study demonstrates the etching of materials resistant to physical sputtering, such as platinum, ruthenium, and tantalum.

It is interesting that often the energy acquired by a cluster in the process of formation during gas expansion through a nozzle is sufficient for the efficient implementation of chemical reactions without additional acceleration. The formation of clusters from a mixture of argon with chlorine trifluoride, which features a high reactivity with silicon, makes it possible to implement the etching of silicon wafers. By choosing the geometry of the mask through which etching occurs and the angle of incidence of neutral clusters, as well as by changing the angle of incidence during etching, one- and two-dimensional micro- and nanostructures of various geometries can be formed: protrusions, combs, and grooves with a high aspect ratio [247, 248], cantilevers [249], etc.

An original atomic layer etching (ALE) technique using cluster oxygen ions was proposed in [250]. Acetic acid was input into the chamber, which was partially adsorbed on the surface of the sample. After that, the chamber was evacuated, and the surface was irradiated with cluster ions. When using clusters with an average size of 2000–3000 atoms per cluster and a sufficiently low energy (about 5 keV), chemical etching occurred, which was limited by the amount of adsorbed acid. After the entire adsorbate layer was removed, the reactive sputtering stopped, and the energy of the clusters was insufficient for noticeable physical sputtering. In [251], acetylacetone vapors were used to implement a similar process.

3.1.4 Implantation of dopants at ultra-shallow depths. The use of beams of accelerated cluster ions makes it possible to implant dopants to shallow depths (a few nm). A method referred to as infusion has been developed for the implantation of B and Ge as cluster ions into silicon substrates. The essence of the method is to prepare a gas mixture of Ar or Xe and a boron- or germanium-containing gas (1–5%), for example, B_2H_6 or GeH_4, to further obtain gas clusters in a supersonic nozzle, then ionize, accelerate, and use them to bombard a silicon substrate. Unlike atomic or molecular ions, a cluster ion contains about 5000 atoms or molecules per unit

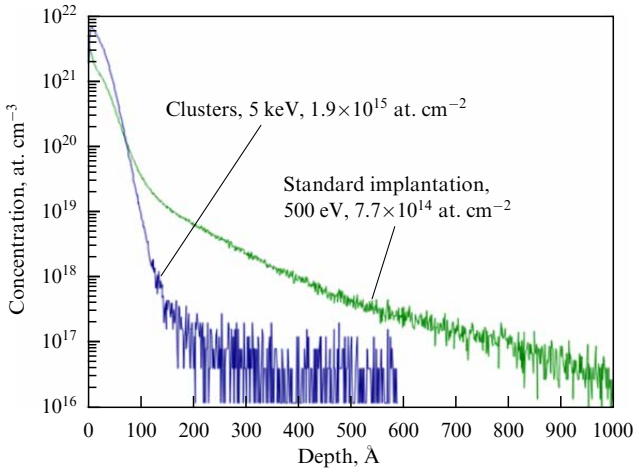

Figure 25. Profiles of the layer-by-layer SIMS analysis of boron in silicon implanted using a monoatomic 500-eV beam of ^{11}B ions and a 5-keV beam of a mixture B_2H_6 and Ar clusters [252].

charge. For a cluster ion energy of 30 keV, the energy per atom or molecule is 6 eV. Controlled implantation of a single boron ion with such an energy is virtually unrealizable. However, within a cluster with such an energy per atom, implantation becomes possible to a depth of several nanometers. In this case, the nature of the interaction of the primary beam with the target material is significantly different. When a cluster collides with a surface, a short-term thermal peak is created at the point of impact, during the lifetime of which (several picoseconds) and under a pressure of hundreds of GPa cluster atoms are implanted into the target.

In addition to the possibility of near-surface implantation, the use of a cluster beam is characterized by the absence of the channeling effect, which can also be explained by the low energy per implanted atom. Figure 25 shows the SIMS profiles for a layer-by-layer analysis of the boron concentration in silicon implanted with a 500-eV monoatomic beam of ^{11}B ions and a 5-keV beam of clusters obtained from a mixture of B_2H_6 and Ar.

A conclusion can be drawn from the profiles shown in Fig. 25 that there is no channeling effect upon implantation with cluster ions. The depth of the p–n junction, i.e., the layer with a boron concentration at the level of 10^{18} cm^{-3}, is 12 nm. In the case of implantation of single boron ions, the depth of the p–n junction due to the channeling effect is equal to 37 nm. In addition, the profile of the distribution of boron implanted by clusters has a steeper slope, which facilitates the creation of impurity distributions with sharper boundaries, and, from an engineering point of view, leads to a decrease in leakage currents and the short channel effect (SCE) of shallow p–n junctions [253].

With an increase in the cluster ion energy E_0, the depth of the p–n junction X_J increases; however, unlike the case of single ions, for which a dependence close to linear is observed, the dependence $X_J \sim E_0^{1/3}$ was experimentally found for clusters. This dependence agrees with the thermal peak model. Since it can be assumed that the volume of silicon involved in the interaction with the cluster is proportional to the energy E_0 of the latter, the linear size of this volume will depend on $E_0^{1/3}$ (the linear size can be understood, for example, as the radius of the hemisphere of the thermal peak core [252, 240]).

Another feature of implantation by cluster ions is the independence of the depth distribution of impurities from their mass. This is a consequence of the collective mechanism of cluster interaction with the surface, in which the main parameters are the total energy and cluster size. Figure 26a shows SIMS profiles of the boron and germanium distribution in silicon upon joint implantation [253].

It should be noted that, despite the high level of argon content in the cluster (95% or more), due to its chemical inertness (high ionization potential), it is rather difficult to detect it in the matrix using SIMS analysis. We can also note the simplicity of controlling the composition of implanted

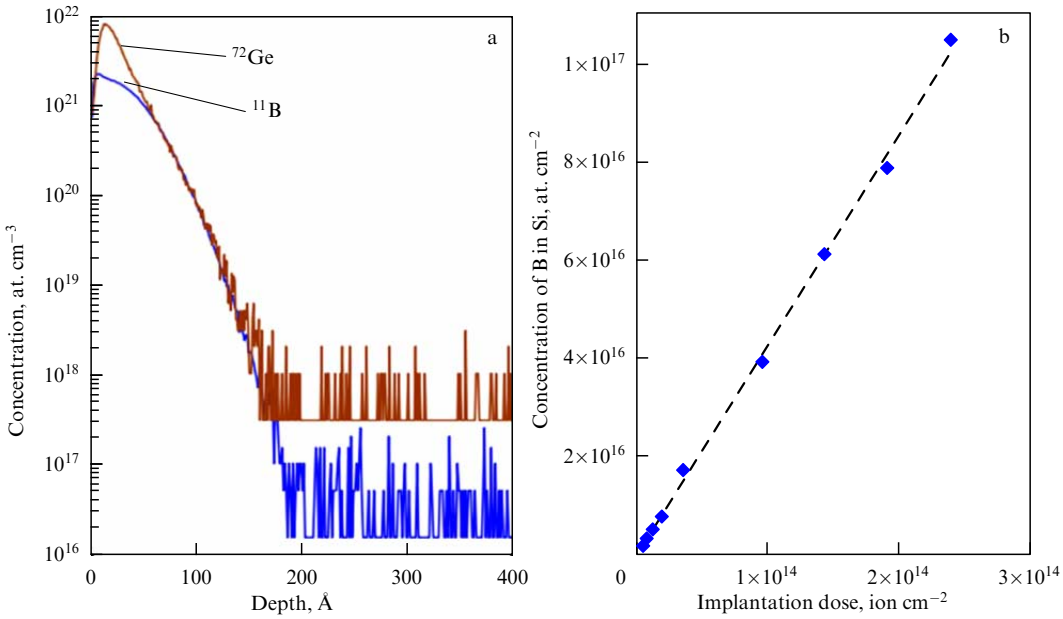

Figure 26. (a) Profiles of layer-by-layer SIMS analysis of boron and germanium in silicon implanted with a 5-keV mixed B_2H_6/Ar and GeH_4/Ar cluster beam. (b) Boron impurity concentration in silicon vs the cluster implantation dose [253].

impurities during joint implantation, which can be carried out by simply varying the ratio of mass flow rates of gas components.

Bombardment of the surface with cluster ions results, as in the case of conventional ion implantation, in amorphization of the near-surface layer; however, unlike standard implantation, due to the low energy per atom, cluster implantation leads to the absence of end-of-range (EOR) defects, which arise at the end of the ion deceleration region after annealing.

The problem of sputtering of the surface layer is well known in conventional ion implantation; it is aggravated with a decrease in the implantation depth. Cluster implantation is not plagued by this shortcoming. A linear relationship between the implantation dose and the impurity concentration in the matrix is observed in wide ranges (Fig. 26b).

If the implantation dose is further increased, the deposition of the material on the surface becomes possible, which was realized for thin films of boron, silicon, germanium, and their mixtures [252]. Thus, the cluster beam combines the capabilities of the technologies of implantation and deposition of thin films [254].

3.2 Surface and thin film analysis

At present, the main methods used for surface and thin film analysis are secondary ion mass spectrometry (SIMS) and X-ray photoelectron spectroscopy. We now consider the advantages that are provided by the use of beams of massive gas cluster ions in these methods.

3.2.1 Mass spectrometry of secondary ions. SIMS is an analytical method based on sputtering the surface of the sample under study with a primary ion beam followed by a mass spectral analysis of the sputtered secondary ions. Detailed information about this method, its physical foundations, and the hardware and applications used can be found, for example, in [255–257].

In its essence, SIMS is a fundamentally destructive method, although the degree of destruction of the surface of the studied samples can be different depending on the modes and goals of the analysis. In the static mode at a current density of less than 5 nA cm^{-2}, elemental, isotopic, and chemical (molecular) analyses of the surface are carried out by measuring the mass spectra of secondary ions, while, in the dynamic mode with a current density in the range of μA cm^{-2}, layer-by-layer analysis (depth profiling) is possible, i.e., the dependences of the intensities of ions with a given m/z ratio on the sputtering time of the sample are measured, followed by conversion of this time into the depth of analysis. A sharply focused ion beam enables obtainment of a local distribution (image or microgram) of the intensities of selected ions over the sample surface, i.e., execution of elemental (chemical) microanalysis and, in combination with layer-by-layer analysis, reconstruction of the spatial distribution of these intensities in the sputtered microvolume of the sample (3D-SIMS).

Historically, the first ion beams that were used in SIMS were those of positive atomic ions of inert gases, primarily argon. Then, to enhance the sensitivity (the limit of detection of impurities), application of positive and negative ions of active elements — oxygen and cesium and complex SF_5^+ ions — began. An improvement in the spatial resolution was achieved due to Ga ions generated by electrohydrodynamic (liquid metal) ion sources [3], while gold and bismuth cluster ions produced by such sources made it possible to increase the sensitivity of the analysis and reduce the fragmentation of sputtered molecular ions. Now, many installations intended for time-of-flight mass spectrometry of secondary ions (TOF-SIMS) use two ion beams (dual-beam mode): one beam (oxygen or cesium ions) sputters the sample in the dynamic mode, while the second, pulsed beam (ions of gold or bismuth, either atomic or cluster), is used to generate an analytical signal of secondary ions. In this way, the dynamic and static regimes are combined, which is typical of state-of-the-art commercial SIMS installations, for example, TOF.SIMS-5 (ION-TOF, Germany).

Sources of C_{60}^+ fullerene ions and complex metal ions, for example, $Os_3(CO)_{12}^+$, have also been developed and successfully tested. It seems promising to use low-temperature ionic liquids [258] and other liquid compounds, primarily water and ethanol, as working substances in ion sources for SIMS. Sources with such working substances can operate both in a purely ionic mode, creating beams of cluster ions of both polarities with a mass of up to several thousand daltons, and in a colloidal (electrospray) mode, generating a stream of charged drops with a diameter of tens of nanometers. Detailed information about various sources of cluster ions and the features of their application in cluster SIMS can be found in [259].

The main advantage provided by the use of massive gas cluster ions is the possibility of molecular layer-by-layer and local microanalysis, including 3D-SIMS, of complex inorganic and organic compounds, including biological objects, at radiation doses greatly exceeding the conventional limit of static analysis. In this case, the original or close to the original molecular compounds with a large mass are retained in the composition of secondary ions, which are usually destroyed (fragmented) when analyzed by a beam of atomic or cluster ions with a small number of atoms in the cluster. Important aspects are the relative smoothness (insignificant roughness) of the bottom of the etching crater under bombardment with a gas cluster ion beam (GCIB) and the absence of microinclusions in the crater associated with implantation/adsorption of primary ions, which allows layer-by-layer analysis to a depth of up to several micrometers while maintaining high depth resolution.

We now consider how GCIB bombardment affects the efficiency of sputtering and the ionization of sputtered particles (ion yield), processes that play the main role in the mass spectrometry of secondary ions. Unlike other cluster ions, GCIBs are formed from a large number of atoms, for example, argon Ar_n^+, where $n \sim 60-5000$, which makes it possible to reduce the specific kinetic energy per atom in a cluster to less than 10 eV at an energy in the beam of 5–30 keV. In this case, the cluster size, i.e., the number of atoms in it, can vary widely, which cannot be attained, for example, in a beam of fullerene ions C_{60}^+.

Computer calculations based on the molecular dynamics method [172] showed a direct dependence of the displacement of silicon atoms and the degree of destruction/disordering of the Si{100} surface on the size of the bombarding argon cluster. For thick films of organic compounds of arginine, leucine, and triglycine, it was found that, if $Ar_{1500-2000}$ beams are used instead of Ar_{300} beams at the same beam energy, the fragmentation of the initial molecules is significantly reduced [260].

For thin films of polystyrene tetramer (PS4) on an Ag{111} surface, it was found in [261] that, upon bombardment with 15-keV Ar_{2953} clusters, the number of sputtered

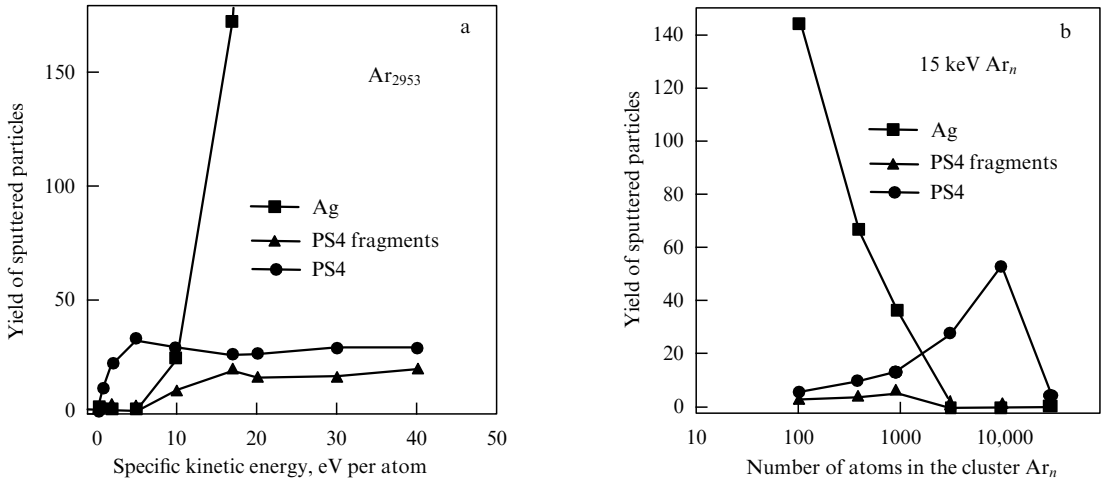

Figure 27. Yield of sputtered silver atoms, molecular fragments, and PS4 molecules themselves emitted from a PS4/Ag {111} system vs (a) the specific kinetic energy of atoms in an Ar_{2953} cluster and (b) the number of atoms in this cluster at a beam energy of 15 keV. Primary beam in both cases is directed along the normal to the surface [261].

initial PS4 molecules is 33 per primary cluster ion, while for C_{60} clusters with the same energy it is only four. It was shown (Fig. 27a) that, if the argon cluster size is fixed, the number of sputtered PS4 molecules increases with increasing energy and reaches saturation at 5 eV per atom; next, fragmentation of these molecules and emission of substrate atoms begin. However, fragmentation and emission of substrate atoms decrease with an increase in the argon cluster size (Fig. 27b), and, at a constant specific energy, a linear dependence of the molecular sputtering efficiency on the number of atoms in the cluster is observed. Two mechanisms of molecular sputtering were proposed for Ar-GCIB beams with an energy corresponding to the saturation regime [261]. According to the first mechanism, the initial molecules are sputtered due to the collective action of argon atoms on them, which results in a shift of these molecules towards the nearest neighboring molecules, which act as a kind of springboard pushing the displaced molecules into a vacuum. Such a mechanism is basically 'operative' for molecules from the uppermost layer. The second mechanism assumes that the role of a springboard for molecules from deeper layers is played by the atoms of the metal substrate along with argon atoms, which, being backscattered from the atoms of the substrate, contribute to the sputtering of organic molecules. The mechanisms for enhancing the yield of secondary ions near the interface were studied in detail in [262].

From a practical perspective, of interest and use is the option to carry out Ar-GCIB-SIMS of complex organic compounds at specific energies of less than 10 eV per atom, i.e., below the classical sputtering threshold [263–265]. It should be noted right away that, if primary C_{60}^+ ions are used, this possibility is absent. Of course, at low energies, the intensity of molecular ion signals decreases; however, the fragmentation of these ions decreases much more strongly, which makes it possible to obtain objective information on the composition of molecules with C–C, C–N, and C–O bonds, the dissociation energies of which do not exceed 3–5 eV. As to the analysis of complex molecular compounds, for example, chymotrypsin, which is a digestive enzymatic component of pancreatic juice, studies [264, 266], which used Ar_{1500}^+ cluster ions with an energy of 5 keV (3.3 eV per atom) without noticeable fragmentation in the mass spectrum of secondary ions, observed peaks of heavy initial molecules with a mass of $\sim 25 \times 10^3$ Da.

At present, there is neither complete clarity nor consensus on the mechanisms of ionization of molecules during the sputtering of organic compounds by massive gas cluster ions. Rabbani et al. [267] showed experimentally that, at a constant beam energy, an approximately linear decrease in the ion yield is observed with an increase in the size of the argon cluster; this is indicative of the impact character of ionization accompanied by electronic excitation of the sputtered molecules. The impact of a macroscopic shock wave [268] and vibrational excitation during local heating [269] are also considered to be probable ionization mechanisms.

This notwithstanding, difficulties in understanding the processes of sputtering and ionization of molecules in Ar-GCIB-SIMS do not adversely affect the practical application of this technique for layer-by-layer analysis. Numerous examples of studies of organic compounds can be found in [270], and of semiconductors and metals, in [271]. It should be noted that, for layer-by-layer analysis, in addition to reducing the degree of fragmentation of the initial molecules, which was discussed above, of special importance becomes the maximum possible depth of 'defect-free' layer-by-layer analysis, i.e., an analysis that does not violate the molecular composition of the analyzed substance and depth resolution. Estimation of the depth of defect-free analysis [270] by GCIB-SIMS of a PMMA polymer compound using cluster beams of $Ar_{n>500}^+$ gives a value of more than 10 μm, which is much greater than the 1.5–2 μm that can be provided with primary C_{60}^+ ions. In this case, the minimum depth resolution for a standard Irganox sample under optimal experimental conditions is 5 nm for argon cluster ions and about 9 nm for fullerene ions. The optimal experimental conditions for layer-by-layer Ar-GCIB-SIMS analysis are the same as those for conventional layer-by-layer analysis using atomic ion beams: the minimum possible energy of the ion beam and its grazing incidence on the surface of a rotating sample.

A comparison of the results of layer-by-layer analysis of various polymeric and biomolecular samples using Ar-GCIB and C_{60}^+ obtained in the same experimental setup showed that the use of massive gas cluster ions provides a 'softer' sputtering mechanism, due to which the accumulation of

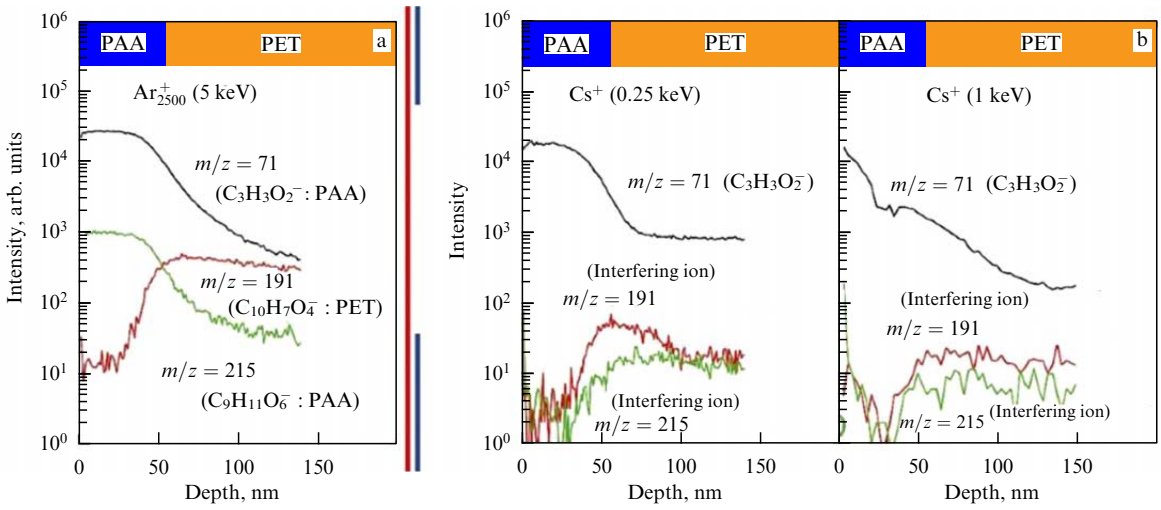

Figure 28. Profiles of layer-by-layer analysis of films of cross-linkable organic materials PAA (polyacrylamide)/PET (polyethylene terephthalate) obtained using Ar^+_{2500} cluster ions with an energy of 5 keV (2.5 eV per atom) (a) and Cs^+ ions with energies of 1 and 0.25 keV (b) [273].

defects in the process of layer-by-layer analysis is reduced. In [272], the 'dual-beam' mode using Ar^+_n beams with an energy of 2–10 eV per atom and C^+_{60} with an energy of 167–667 eV per atom for sputtering of polymer samples (in both cases, the analysis was carried out with 30-keV Bi^+_3 ions) was used to find that Ar-GCIB bombardment provides a high yield of molecular ions from the beginning to the end of layer-by-layer analysis at a sputtering threshold in the range of 1–1.7 eV per atom. These results enable reaching a conclusion that massive gas cluster ions are a more versatile ion probe than a fullerene ion beam both for 'sputter–analysis' with a single ion beam and in the two-beam mode, when Ar^+_n and C^+_{60} are only used for sputtering samples.

The difference is even more noticeable if comparing Ar-GCIB with atomic ion beams. Figure 28 [273] shows the results of a layer-by-layer analysis of films of cross-linkable organic materials PAA (polyacrylamide)/PET (polyethylene terephthalate) using Ar^+_{2500} cluster ions with an energy of 5 keV (2.5 eV per atom) and Cs^+ ions with energies of 1 and 0.25 keV. Negative molecular ions $C_3H_3O_2$ ($m/z = 71$) and $C_9H_{11}O_6$ ($m/z = 215$) were registered as characteristic secondary ions for PAA, and $C_{10}H_7O_4$ ($m/z = 191$), for PET. Figure 28 shows that, even at an energy of 0.25 keV with a beam of cesium ions for PAA, it is only possible to obtain the distribution profile of light $C_3H_3O_2$ ions, while for heavier molecular ions, for samples of both PAA and PET, their profiles are practically absent due to fragmentation of the original molecules, which is not observed when using Ar-GCIB.

The substance sputtered from the target during the analysis by the SIMS method is usually not studied further. However, it was proposed in [274] to use the deposit obtained on a substrate during sputtering of various organic materials by cluster ions for a more accurate determination of the chemical structure and molecular weight distribution of polymers. Pyrolytic gas chromatography and matrix-assisted laser desorption/ionization (MALDI) were applied to show that, despite the molecular weight distribution of the precipitate being slightly shifted to the low-mass region, bombardment with cluster ions only led to relatively weak fragmentation of sputtered molecules. Thus, it becomes possible to transfer large organic molecules from the reservoir sample to the substrate [275]; for example, study [276] demonstrated ion-cluster precipitation of proteins with preservation of their enzymatic activity.

We now discuss shortcomings of Ar-GCIB-SIMS and ways to eliminate them. The main drawback is the low ion yield, which reduces the sensitivity of the method. Since an increase in the ion yield due to an increase in the efficiency of sputtering negates the main advantage of this method, the low fragmentation of initial organic molecules, the only possible way is to increase the efficiency of ionization of sputtered molecules. Various methods are used to this end, including flooding of the surface of the samples under study with water molecules [277] and bombardment with cluster beams of H_2O^+ ions [278].

It is very promising to add molecules of reactive compounds to the composition of argon cluster beams, i.e., create combined heterogeneous cluster beams. In this case, the reactive additive as part of the primary ion beam is locally delivered to a specified location on the surface of the sample under study, and upon interaction of the cluster with the surface, it is activated and contributes to an increase in the efficiency of ionization of the sputtered molecules. The concentration of reactive additives in the ion beam can vary over a wide range, but in any case it remains low enough not to cause contamination of the surface under study or disturb the vacuum conditions in the ion source. Compounds CH_4 [279], H_2O [280], and HCl [281] are currently used as such additives, which are introduced in the gas or vapor phase into the ionization chamber of an ion source at a relative partial pressure of 1–5% of argon pressure. They are then embedded in the structure of an argon cluster, and the resulting heterogeneous cluster is ionized by an electron beam. Study [282] examined the potential of a source of clusters based on a mixture of argon and carbon dioxide to show that, at a CO_2 concentration of 95%, the yield of secondary ions of organic materials is doubled compared to pure argon clusters.

Figure 29 [281] shows the results of a layer-by-layer analysis in positive and negative secondary ions of thin D_2O ice layers on the surface of a film of trehalose (mycosis), an organic compound from the group of disaccharides with the formula $C_{12}H_{22}O_{11}$ and a molecular weight of 342 Da. Homogeneous Ar^+_{2000} and heterogeneous cluster ions $[Ar + HCl]^+_{2000}$ were used as primary ions. The beam energy

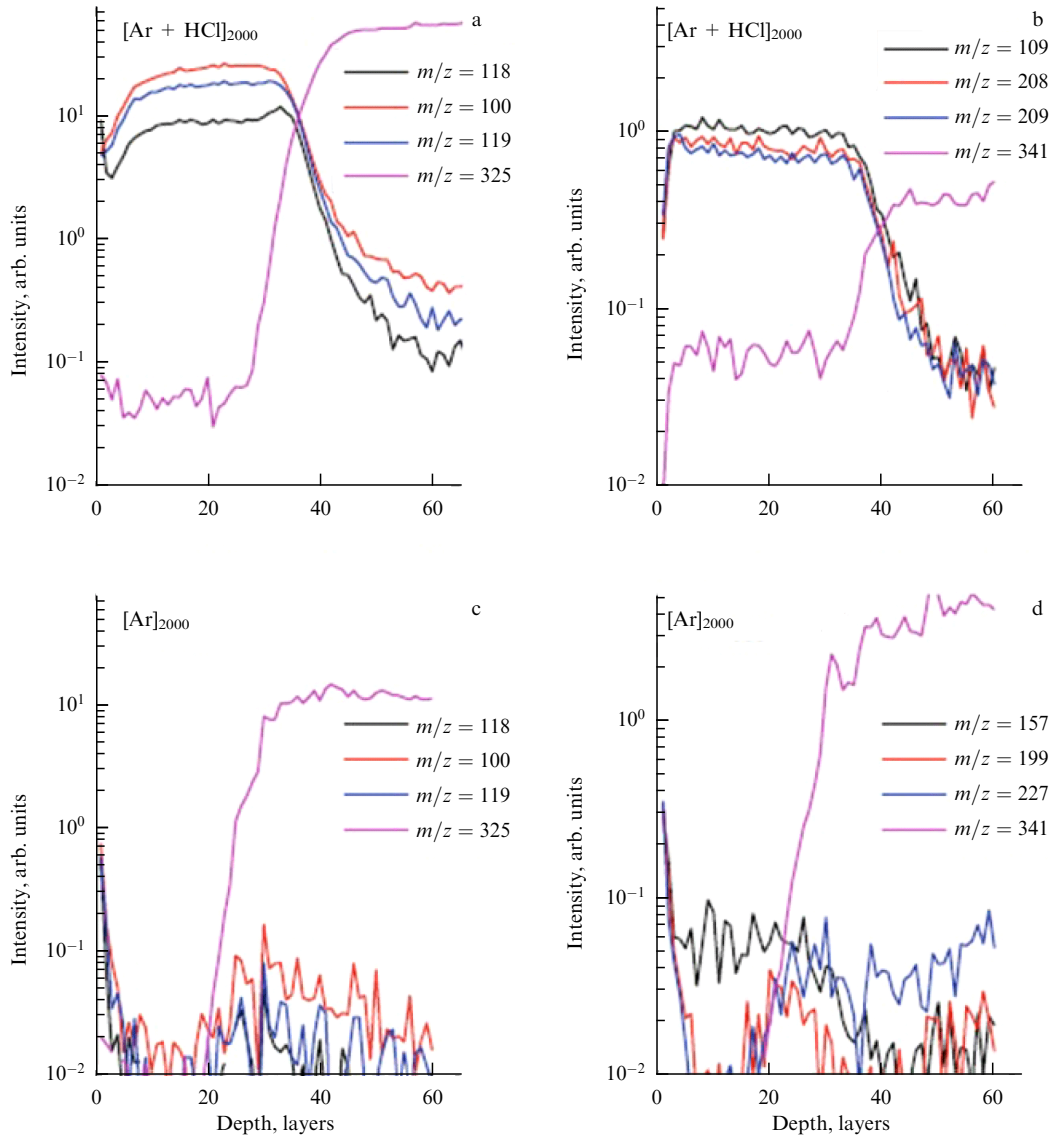

Figure 29. Profiles of layer-by-layer analysis of thin D_2O ice layers on the surface of a trehalose film obtained with positive (a, c) and negative (b, d) secondary ions upon bombardment with heterogeneous clusters $[Ar + HCl]^+_{2000}$ (a, b) and homogeneous clusters Ar^+_{2000} (c, d). Energy of the primary ion beam in both cases was 20 keV [281].

in both cases was 20 keV, and the concentration of hydrochloric acid vapor in the ionization chamber did not exceed 5%. Positive $[M-OH]^+$ ions with $m/z = 325$ and negative $[M-H]^-$ ions with $m/z = 341$, where M is a trehalose molecule, were chosen as characteristic secondary ions for trehalose. For ice layers, positive ions $[D_2O]^+_n$, $[D_2O]_nH^+$, and $[D_2O]_nD^+$ were registered, the profiles of which are shown in Fig. 29a, c, and negative ions $[D_2O]_nO^-$, $[D_2O]_nOH^-$, and $[D_2O]_nOD^-$, the profiles of which are shown in Fig. 29b, d. It can be seen in Fig. 29 that the use of a reactive additive of hydrochloric acid vapor in the composition of the primary cluster beam significantly increases the intensity of the characteristic ice ions and makes it possible to measure their profiles in both positive and negative secondary ions, which cannot be done when bombarded by a beam of homogeneous argon clusters.

A promising area is the development of a heterogeneous cluster ion source [283], which is a combination of a gas-dynamic source and a source based on low-temperature ionic liquids (LTILs) [258]. In such a device, there is no need for a cluster beam ionizer, since the generation of cluster ions occurs due to the introduction of an LTIL ion into a neutral gas cluster. In this case, it is possible to create both positively and negatively charged massive gas clusters with a reactive addition of LTIL cations or anions, the set of ions being the most diverse, given the large number of ionic liquids (more than 5000 at present) with various chemical activities and masses of cations/anions.

The disadvantage of the GCIB-SIMS method is also its low locality, i.e., a relatively large diameter of the ion beam on the surface of the sample, the value of which is usually tens of microns. Difficulties in obtaining a sharply focused ion beam are due to the fact that neutral gas clusters are ionized by electrons, and the ionization region cannot be localized to a point with high brightness and a small spread in initial energy, as in the case of liquid-metal ion sources [3], where the ion beam can be focused to a diameter of less than 10 nm. Nevertheless, methods of local GCIB-SIMS and 3D-GCIB-SIMS are being developed, in which a cluster beam of argon ions is used for sputtering, while the analytical signal is

Figure 30. External view of J105 3D Chemical Imager (Ionoptika, UK), a cluster TOF-SIMS microanalyzer [286].

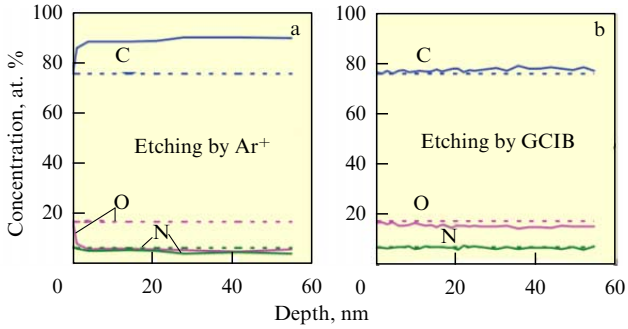

Figure 31. XPS depth profiling of a polyimide film sputtered with Ar^+ atomic ions (a) and Ar_n^+ cluster ions (b). Dashed lines show the atomic concentration of carbon, oxygen, and nitrogen that corresponds to the stoichiometric composition of the polyimide. Sputtering depth was calculated using the sputtering rate of SiO_2 [292].

formed by a sharply focused beam of Bi_3^+ ions. Examples of microanalysis of various biological objects, including 3D results, together with a discussion of the features of the reconstruction of experimental data, can be found, for example, in [284, 285]. It should be noted that, in studying biomolecular objects, due to their specific structure, it is rather difficult to calibrate the sputtering depth.

UK-based Ionoptika has developed the J105 3D Chemical Imager, a specialized device for TOF-SIMS cluster microanalysis [286–288]. An image of this device is shown in Fig. 30. It is equipped with two ion sources, which make it possible to obtain massive cluster beams of water and argon ions, including those with reactive additives, with an energy of 20 keV and a beam diameter of about 30 μm, a system for cooling samples to 100 K, and a box for samples sensitive to the effects of air and water vapor. One of the main features of the J105 3D is the ability to operate with ion sources in the DC mode for GCIB-TOF-SIMS, since the time-of-flight analyzer is equipped with a special device for modulating the secondary ion beam. This option significantly reduces analysis time compared to conventional TOF-SIMS analyzers that use pulsed primary ion beams. For example, an analysis of 10^8 molecules in a volume pixel (voxel) with dimensions of 1 μm × 1 μm × 10 nm using a pulsed ion beam with a current of 0.01 nA at a pulse duration of 100 ns and a repetition rate of 10 kHz in a conventional analyzer takes 10 s. Obtaining a 3D micrograph with a size of 256 × 256 voxels would then take at least 180 hours, while the J105 3D setup only needs 11 minutes.

3.2.2 X-ray photoelectron spectroscopy. XPS is currently the most common method used for elemental and chemical analysis of surfaces and thin films. It is based on the phenomenon of an external photoelectric effect that occurs when an object under study is irradiated with a soft X-ray beam. Detailed information about the XPS method, its hardware, and applications can be found, for example, in [289–291].

In XPS devices, a beam of massive gaseous cluster ions is only used for layer-by-layer sputtering or surface cleaning of the objects under study. In this case, the main advantage of Ar-GCIB is realized: sputtering occurs with minimal roughness of crater bottom etching and minimal destruction of the chemical (molecular) structure of both inorganic and organic materials.

Figure 31 displays as an example the results of layer-by-layer XPS analysis of a polyimide film using atomic (Fig. 31a) and massive cluster (Fig. 31b) argon ions. It can be seen that, upon sputtering with atomic ions, the ratio of carbon and oxygen concentrations is violated, while, upon Ar-GCIB sputtering, it remains close to the values that correspond to the stoichiometric composition of the polyimide. The results of XPS studies of silicon dioxide layers on the surface of silicon substrates using Ar-GCIB sputtering are presented in [293], layer-by-layer analysis of GaP/Si(001) heterostructures is discussed in [294], and an increase in the corrosion resistance of a brass surface with the use of organic inhibitors was studied in [295]. Study [296] compared the change in the hybridization of carbon atoms in graphite materials upon etching with atomic argon and Ar_{2000}^+ clusters. Cluster etching resulted in a much smaller deviation of the sp^2/sp^3 ratio from the initial value; moreover, in this case, no effect of implanted argon atoms on the XPS spectra was found. In all studies, the use of massive gas argon cluster beams made it possible to increase the reliability of the chemical XPS.

It should be emphasized that the smoothness of the etching crater bottom, which is necessary for the implementation of high depth resolution, is provided under two conditions: the normal incidence of the cluster flux on the analyzed surface (in the case of tilted incidence, a wavelike relief develops) and a fairly low kinetic energy of the cluster atoms (otherwise, the relief may emerge as a result of overlapping of craters from individual collisions of clusters with the surface). It was shown in [189] that, under normal incidence of 10-keV Ar_{2000}^+ clusters, a difference between the compositions of the Z^+ and Z^- lithium niobate surfaces (positive and negative polar surfaces) is realized, which is close to the theoretical one, i.e., a 'perfect' surface can be obtained.

It should be noted that at present commercial XPS spectrometers are not equipped with Ar-GCIB sources, but they can be installed as an optional addition (see, for example, information about the EnviroESCA spectrometer [297]). It can be expected that in the years to come cluster ion sources will become an essential component of XPS spectrometers.

3.2.3 Determination of local mechanical properties of the surface. Traditional methods for measuring the hardness of materials are based on determining the geometric characteristics of the depression left by a specially shaped indenter pressed into the material. However, in measuring the hardness of films, this method can result in significant error due to the influence of the substrate. Moreover, the sizes of micro- and nanosystems may be too small in other directions for such a method to be applicable. Therefore, a method has been proposed to determine the local hardness of materials, which

is based on measuring the size of craters created by the collision of cluster ions with the surface [298].

The depth of the crater h left on the target surface by a hypersonic macroscopic projectile with a diameter D_p is related to the energy of the projectile (in erg units) and the Brinell hardness (in kg mm^{-2}) by the following formula (at projectile velocities less than 10 km s^{-1}) [298, 299]:

$$\frac{h}{D_p} = \left(\frac{12 \times 10^{-9}(E/B)}{2\pi D_p^3}\right)^{1/3}. \quad (21)$$

For craters left on the target surface by accelerated cluster ions, a correlation was also revealed between the crater diameter and depth and Brinell hardness: $d \sim h \sim B^{-1/3}$ for simple metals (Cu, Ag, Au, Zr); the form of calibration curves for determining the hardness from the crater depth at various cluster energies was proposed [298]. The same study found some regularities in the formation of craters. Study [300] revealed a correlation between the crater diameter and the Vickers hardness for gold, FeCo, SiO_2, and Al_2O_3. A method to determine local hardness based on the correlation between the sputtering coefficient and hardness upon sputtering with atomic cesium ions was developed in [301].

It is clear that, to observe craters, the radiation doses should be low enough to avoid their overlap (i.e., they should not exceed $10^{12}-10^{13}$ ion cm^{-2}). In addition, an error can arise if the source generates multiply charged clusters, such that the energy of such clusters after acceleration is higher than that of singly charged ones and, consequently, they produce craters of a larger volume [112].

Another method to determine the local mechanical properties of the target is based on the observation of the mass spectra of ions of a cluster substance escaping from the collision region: the nature of cluster dissociation upon collision is determined, among other things, by the elastic properties of the target. It can be asserted that, the harder the target, the more easily the cluster is destroyed. For a quantitative description of dissociation, a parameter can be introduced which is the ratio of the intensity of the peak of secondary ions of cluster substance dimers (for example, argon) and the total intensity of all peaks of all secondary argon clusters $\eta_{di} = Ar_2^+ / \sum Ar_n^+$. Study [302] discovered a dependence close to linear between Young's modulus of the target (Ag, Cu, Au, Pt, W) and η_{di}. A similar method was used to determine the glass transition temperature of the surface of polymer films [303, 304]: the nature of the emission of secondary argon clusters changed quite sharply near the transition temperature.

4. Conclusions

In this analytical review, we made an attempt to cover a wide range of problems and issues related to the formation of beams of neutral gas clusters, their diagnostics, ionization, and mass separation. The main design features of state-of-the-art gas-dynamic sources of cluster ions intended for technological and analytical applications are considered. Particular attention is paid to modern areas of GCIB application, which cover precision polishing and the formation of an ordered surface relief, modification of the chemical properties of the surface, and implantation at ultra-shallow depths. The analysis of the surface and thin films, including organic ones, by secondary ion mass spectrometry and X-ray photoelectron spectroscopy using gas cluster ions, and the determination of the local mechanical properties of the surface, are presented in the review.

From a philosophical perspective (according to Aristotle, philosophy is the queen of sciences), the interaction of massive gas cluster ions with a surface can be considered a manifestation of the dialectical law of the transition of quantitative changes into qualitative ones. An increase in the cluster ion size, i.e., the number of atoms in its composition, while maintaining its kinetic energy, leads to a decrease in the specific energy per atom in the cluster, and this, in turn, makes it possible to lower the sputtering threshold and facilitates the development of nonlinear cascades of collisions and thermal peaks, which ultimately enables super-precision surface polishing, molecular chemical analysis of organic compounds, and many other processes which are unattainable using conventional atomic ion beams. We hope that our review will draw the attention of Russian scientists to the design and application of gas-dynamic sources of cluster ions and contribute to the development of this discipline and its implementation in scientific research and engineering applications.

Acknowledgments. The study was financially support by the Russian Foundation for Basic Research (project no. 20-18-50253).

References

1. Brown I G (Ed.) *The Physics and Technology of Ion Sources* (New York: John Wiley and Sons, 1989); Translated into Russian: *Fizika i Tekhnologiya Istochnikov Ionov* (Moscow: Mir, 1998)
2. Dudnikov V G *Phys. Usp.* **62** 1233 (2019); *Usp. Fiz. Nauk* **189** 1315 (2019)
3. Mazarov P, Dudnikov V G, Tolstoguzov A B *Phys. Usp.* **63** 1219 (2020); *Usp. Fiz. Nauk* **190** 1293 (2020)
4. Kantrowitz A, Grey J *Rev. Sci. Instrum.* **22** 328 (1951)
5. Kistiakowsky G B, Slichter W P *Rev. Sci. Instrum.* **22** 333 (1951)
6. Henkes W *Z. Naturforsch. A* **16** 842 (1961)
7. Bentley P G *Nature* **190** 432 (1961)
8. Hagena O-F, Henkes W *Z. Naturforsch. A* **20** 1344 (1965)
9. Becker E W et al. "Development and construction of an injector using hydrogen cluster ions for nuclear fusion devices", Kernforschungszentrum Karlsruhe KFK 2016 (Karlsruhe: Gesellschaft für Kernforschung M.B.H., 1974) Status Report as of December 1973
10. Henkes W P R, Klingelhöfer R *J. Phys. Colloques* **50** C2-159 (1989)
11. Henkes P R W *Rev. Sci. Instrum.* **61** 360 (1990)
12. Yamada I *AIP Conf. Proc.* **1321** 1 (2011)
13. Anderson J B, Fenn J B *Phys. Fluids* **8** 780 (1965)
14. Eletskii A V, Smirnov B M *Sov. Phys. Usp.* **32** 763 (1989); *Usp. Fiz. Nauk* **159** 45 (1989)
15. Makarov G N *Phys. Usp.* **49** 117 (2006); *Usp. Fiz. Nauk* **176** 121 (2006)
16. Karpenko Yu A, Baturin V A *Zh. Nanoelektron. Fiz.* **4** (3) 03015 (2012)
17. Smirnov B M *Phys. Usp.* **46** 589 (2003); *Usp. Fiz. Nauk* **173** 609 (2003)
18. Andreev A A et al. *Nanotekhnol. Razrabotka, Primenenie XXI Vek* **1** (1) 23 (2009)
19. Avduevskii V S et al. *Gazodinamika Sverkhzvukovykh Neizobaricheskikh Strui* (Gas Dynamics of Supersonic Nonisobaric Jets) (Moscow: Mashinostroenie, 1989)
20. Pauly H *Atom, Molecule, and Cluster Beams* Vol. 2 (Berlin: Springer, 2000)
21. Campargue R (Ed.) *Atomic and Molecular Beams: the State of the Art 2000* (Berlin: Springer, 2001)
22. Scoles G (Ed.) *Atomic and Molecular Beam Methods* Vol. 1 (New York: Oxford Univ. Press, 1988)
23. Scoles G (Ed.) *Atomic and Molecular Beam Methods* Vol. 2 (New York: Oxford Univ. Press, 1992)

24. Aleksandrov M L, Kusner Yu S *Gazodinamicheskie, Molekulyarnye, Ionnye i Klastirovannye Puchki* (Gas Dynamic, Molecular, Ion, and Clustered Beams) (Leningrad: Nauka, 1989)
25. Hagena O F, Obert W *J. Chem. Phys.* **56** 1793 (1972)
26. Lu H et al. *J. Chem. Phys.* **132** 124303 (2010)
27. Chen G et al. *J. Appl. Phys.* **108** 064329 (2010)
28. Korobeishchikov N G et al. *Vacuum* **119** 256 (2015)
29. Dulov V G, Luk'yanov G A *Gazodinamika Protsessov Istecheniya* (Gas Dynamics of Outflow Processes) (Novosibirsk: Nauka, 1984)
30. Ashkenas H, Sherman F S, in *Rarefied Gas Dynamics. Proc. of the Fourth Intern. Symp., Toronto, 1964* Vol. 2 (Ed. J H de Leeuw) (New York: Academic Press, 1965) p. 84
31. Crist S, Sherman P M, Glass D R *AIAA J.* **4** 68 (1966)
32. Beijerinck H C W et al. *Chem. Phys.* **96** 153 (1985)
33. van Eck H J N *J. Appl. Phys.* **105** 063307 (2009)
34. Zarvin A E, Sharafutdinov R G *J. Appl. Mech. Tech. Phys.* **20** 744 (1979); *Priklad. Mekh. Tekh. Fiz.* (6) 107 (1979)
35. Campargue R *J. Phys. Chem.* **88** 4466 (1984)
36. Weaver B D, Frankl D R *Rev. Sci. Instrum.* **58** 2115 (1987)
37. Lewis C H, Carlson D J *AIAA J.* **2** 776 (1964)
38. Hagena O F *Rev. Sci. Instrum.* **63** 2374 (1992)
39. Even U *Adv. Chem.* **2014** 636042 (2014)
40. Chekmarev S F, Stankus N V *Sov. Phys. Tech. Phys.* **29** 920 (1984); *Zh. Tekh. Fiz.* **54** 1576 (1984)
41. Korobeishchikov N G, Zarvin A E, Madirbaev V Z *Tech. Phys.* **49** 973 (2004); *Zh. Tekh. Fiz.* **74** (8) 21 (2003)
42. Dimov G I *Prib. Tekh. Eksp.* (5) 168 (1968)
43. Christen W, Rademann K, Even U *J. Chem. Phys.* **125** 174307 (2006)
44. Irimia D et al. *Rev. Sci. Instrum.* **80** 113303 (2009)
45. Popok V N et al. *Rev. Sci. Instrum.* **73** 4283 (2002)
46. Andreev A A et al. *Vacuum* **91** 47 (2013)
47. Zeng X M et al. *Chinese Phys. C* **41** 087003 (2017)
48. Ieshkin A E, Ermakov Y A, Chernysh V S *Tech. Phys. Lett.* **41** 1072 (2015); *Pis'ma Zh. Tekh. Fiz.* **41** (22) 8 (2015)
49. Bier K, Schmidt B *Z. Angew. Phys.* **13** 496 (1961)
50. Zarvin A E et al. *Tech. Phys. Lett.* **41** 1103 (2015); *Pis'ma Zh. Tekh. Fiz.* **41** (22) 74 (2015)
51. Ieshkin A et al. *Nucl. Instrum. Meth. Phys. Res. A* **795** 395 (2015)
52. Ieshkin A E et al. *J. Vis.* **22** 741 (2019)
53. Kislyakov N I, Rebrov A K, Sharafutdinov R G *J. Appl. Mech. Tech. Phys.* **16** 187 (1975); *Priklad. Mekh. Tekh. Fiz.* (2) 42 (1975)
54. Zarvin A E, Yaskin A S, Kalyada V V *J. Appl. Mech. Tech. Phys.* **59** 86 (2018); *Priklad. Mekh. Tekh. Fiz.* (1) 99 (2018)
55. Wegner K et al. *J. Phys. D* **39** R439 (2006)
56. Hagena O F *Phys. Fluids* **17** 894 (1974)
57. Hagena O F *Surf. Sci.* **106** 101 (1981)
58. Hagena O F *Z. Phys. D* **4** 291 (1987)
59. Korobeishchikov N G, Roenko M A, Tarantsev G I *J. Clust. Sci.* **28** 2529 (2017)
60. Smith R A, Ditmire T, Tisch J W G *Rev. Sci. Instrum.* **69** 3798 (1998)
61. Sharma P K, Knuth E L, Young W S *J. Chem. Phys.* **64** 4345 (1976)
62. Buck U, Krohne R *J. Chem. Phys.* **105** 5408 (1996)
63. Karnbach R et al. *Rev. Sci. Instrum.* **64** 2838 (1993)
64. Korobeishchikov N G et al. *Plasma Chem. Plasma Process.* **25** 319 (2005)
65. Zarvin A E et al. *Eur. Phys. J. D* **49** 101 (2008)
66. Winkler M, Harnes J, Børve K J *J. Phys. Chem. A* **115** 13259 (2011)
67. Lundwall M et al. *J. Chem. Phys.* **126** 214706 (2007)
68. Nagasaka M et al. *J. Chem. Phys.* **137** 214305 (2012)
69. Pysanenko A et al. *Int. J. Mass Spectrom.* **461** 116514 (2021)
70. Shyrokorad D, Kornich G, Buga S *Mater. Today Commun.* **23** 101107 (2020)
71. Yamada I et al. *Mater. Sci. Eng. A* **253** 249 (1998)
72. Bell A J et al. *J. Phys. D* **26** 994 (1993)
73. Bush A M et al. *J. Phys. Chem. A* **102** 6457 (1998)
74. Ditmire T et al. *Phys. Rev. A* **53** 3379 (1996)
75. Ramos A et al. *Phys. Rev. A* **72** 053204 (2005)
76. Kim K Y, Kumarappan V, Milchberg H M *Appl. Phys. Lett.* **83** 3210 (2003)
77. Gupta K C et al. *J. Appl. Phys.* **118** 114308 (2015)
78. Dorchies F et al. *Phys. Rev. A* **68** 023201 (2003)
79. Wörmer J, Joppien M, Möller T *Chem. Phys. Lett.* **182** 632 (1991)
80. Tchaplyguine M et al. *J. Chem. Phys.* **120** 345 (2004)
81. Amar F G, Smaby J, Preston T J *J. Chem. Phys.* **122** 244717 (2005)
82. Harnes J et al. *J. Phys. Chem. A* **115** 10408 (2011)
83. Bonnamy A et al. *J. Chem. Phys.* **118** 3612 (2003)
84. Bonnamy A et al. *Phys. Chem. Chem. Phys.* **7** 963 (2005)
85. Farges J et al. *J. Chem. Phys.* **84** 3491 (1986)
86. Danil'chenko A G, Kovalenko S I, Samovarov V N *Low Temp. Phys.* **35** 965 (2009); *Fiz. Nizk. Temp.* **35** 1240 (2009)
87. De Martino A et al. *Z. Phys. D* **27** 185 (1993)
88. Fedor J et al. *J. Chem. Phys.* **135** 104305 (2011)
89. Korobeishchikov N G, Penkov O I *Vacuum* **125** 205 (2016)
90. Soler J M *Phys. Rev. Lett.* **49** 1857 (1982)
91. Schütte S, Buck U *Int. J. Mass Spectrom.* **220** 183 (2002)
92. Song J H et al. *Nucl. Instrum. Meth. Phys. Res. B* **179** 568 (2001)
93. Ryuto H et al. *Vacuum* **84** 505 (2009)
94. Echt O et al. *Z. Phys. B Cond. Matter* **53** 71 (1983)
95. Söderlund J et al. *Phys. Rev. Lett.* **80** 2386 (1998)
96. Rupp D et al. *J. Chem. Phys.* **141** 044306 (2014)
97. Bobbert C et al. *Eur. Phys. J. D* **19** 183 (2002)
98. Korobeishchikov N G, Nikolaev I V, Roenko M A *J. Phys. Conf. Ser.* **1115** 032016 (2018)
99. Gao X et al. *J. Appl. Phys.* **114** 034903 (2013)
100. Jang D G et al. *Appl. Phys. Lett.* **105** 021906 (2014)
101. Vostrikov A A, Dubov D Yu *J. Exp. Theor. Phys.* **98** 197 (2004); *Zh. Eksp. Teor. Fiz.* **125** 222 (2004)
102. Anisimov M P *Russ. Chem. Rev.* **72** 591 (2003); *Usp. Khim.* **72** 664 (2003)
103. Boldarev A S et al. *Rev. Sci. Instrum.* **77** 083112 (2006)
104. Korobeishchikov N G et al. *AIP Conf. Proc.* **1628** 885 (2014)
105. Tao Y et al. *J. Appl. Phys.* **119** 164901 (2016)
106. Nazarov V S et al. *J. Phys. Conf. Ser.* **1250** 012026 (2019)
107. Even U *EPJ Techn. Instrum.* **2** 17 (2015)
108. Mack M E "Ionizer and method for gas-cluster ion-beam formation", Patent US 7,173,252 B2 (2007)
109. Lee S J et al. *Bull. Korean Chem. Soc.* **40** 877 (2019)
110. Seki T et al. *Nucl. Instrum. Meth. Phys. Res. B* **206** 902 (2003)
111. Swenson D R *Nucl. Instrum. Meth. Phys. Res. B* **222** 61 (2004)
112. Toyoda N, Yamada I *Nucl. Instrum. Meth. Phys. Res. B* **307** 269 (2013)
113. Scheier P, Märk T D *J. Chem. Phys.* **86** 3056 (1987)
114. Scheier P, Märk T D *Chem. Phys. Lett.* **136** 423 (1987)
115. Pelenovich V O et al. *J. Synch. Investig.* **13** 344 (2019); *Poverkhnost'. Rentgen. Sinkhrotron. Neitron. Issled.* (4) 84 (2019)
116. SIMION, https://simion.com
117. Ono L K "Study of secondary ion emission from Si target bombarded by large cluster ions", M D Thesis (Kyoto: Kyoto Univ., 2004)
118. Bakun A D et al., in *Vzaimodeistvie Ionov s Poverkhnost'yu. VIP-2019. Trudy XXIV Mezhdunarodnoi Konf., 19–23 Avgusta 2019 g., Moskva, Rossiya* (Interaction of Ions with Surface VIP-2019 Proc. 24th Intern. Conf. August 19–23, 2019, Moscow, Russia) Vol. 1 (Eds E Yu Zykova et al.) (Moscow: National Research Nuclear Univ. MEPhI, 2019) p. 84
119. Fujii M et al. *Rapid Commun. Mass Spectrom.* **28** 917 (2014)
120. Mohammadi A S et al. *Anal. Bioanal. Chem.* **408** 6857 (2016)
121. MacCrimmon R et al. *Nucl. Instrum. Meth. Phys. Res. B* **242** 427 (2006)
122. Toyoda N, Isogai H, Yamada I *AIP Conf. Proc.* **1066** 431 (2008)
123. Paruch R J, Postawa Z, Garrison B J *J. Vac. Sci. Technol. B* **34** 03H105 (2016)
124. Toyoda N, Houzumi S, Yamada I *Nucl. Instrum. Meth. Phys. Res. B* **242** 466 (2006)
125. Seliger R L *J. Appl. Phys.* **43** 2352 (1972)
126. Solov'ev A V, Tolstoguzov A B *Sov. Phys. Tech. Phys.* **32** 580 (1987); *Zh. Tekh. Fiz.* **57** 953 (1987)
127. Moritani K et al. *Appl. Surf. Sci.* **255** 948 (2008)
128. Ohwaki K et al. *Nucl. Instrum. Meth. Phys. Res. B* **241** 614 (2005)
129. Moritani K et al. *Nucl. Instrum. Meth. Phys. Res. B* **432** 1 (2018)
130. Anai Y et al. *E-J. Surf. Sci. Nanotechnol.* **14** 161 (2016)
131. Niehuis E et al., in *Secondary Ion Mass Spectrometry SIMS V* (Springer Series in Chemical Physics, Vol. 44, Eds A Benninghoven et al.) (Berlin: Springer-Verlag, 1986) p. 188
132. Kayser S et al. *Surf. Interface Anal.* **45** 131 (2013)

133. Yang L, Seah M P, Gilmore I S *J. Phys. Chem. C* **116** 23735 (2012)
134. Pelenovich V et al. *Vacuum* **172** 109096 (2020)
135. https://www.exogenesis.us/naccel-100-specifications
136. Kirkpatrick A et al. *Nucl. Instrum. Meth. Phys. Res. B* **307** 281 (2013)
137. De Vido M et al. *Opt. Mater. Express.* **7** 3303 (2017)
138. https://www.phi.com/news/introducing-the-gas-cluster-ion-beam-ion-gun.html
139. IONOPTIKA. GCIB 40, https://www.ionoptika.com/products/ion-beams/gas-cluster-ion-beams/gcib-40
140. Winograd N *Annu. Rev. Anal. Chem.* **11** 29 (2018)
141. Zeng X M et al. *Acta Phys. Sin.* **69** 093601 (2020)
142. Kireev D S et al. *Vestn. Ryazanskogo Gos. Radiotekh. Univ.* (66-2) 40 (2018)
143. SRIM, http://www.srim.org
144. Matsuo J et al. *Nucl. Instrum. Meth. Phys. Res. B* **121** 459 (1997)
145. Yamamura Y, Tawara H *At. Data Nucl. Data Tables* **62** 149 (1996)
146. Toyoda N et al. *Mater. Chem. Phys.* **54** 262 (1998)
147. Chernysh V S et al. *Surf. Coat. Technol.* **388** 125608 (2020)
148. Yamada I et al. *Nucl. Instrum. Meth. Phys. Res. B* **164** 944 (2000)
149. Insepov Z, Yamada I, Sosnowski M *Mater. Chem. Phys.* **54** 234 (1998)
150. Kargin N I *Nauch. Vizualizatsiya* **9** (3) 28 (2017)
151. Chainikova A S et al. *Trudy Vseross. Nauchno-Issled. Inst. Aviatsionnykh Mater.* (11) 4 (2015)
152. Ieshkin A et al. *Surf. Topogr. Metrol. Prop.* **7** 025016 (2019)
153. Chirkin M V, Molchanov A V, Serebryakov A E, in *Proc. of the 5th Intern. Conf. on Optical Measurement Techniques for Structures and Systems* (Eds J Dirckx, J Buytaert) (Maastricht: Shaker Publ. BV, 2013) p. 93
154. Akizuki M et al. *Nucl. Instrum. Meth. Phys. Res. B* **99** 229 (1995)
155. Henkes P R W, Krevet B *J. Vac. Sci. Technol. A* **13** 2133 (1995)
156. Yamada I et al. *Mater. Sci. Eng. R* **34** 231 (2001)
157. Ieshkin A E et al. *Surf. Sci.* **700** 121637 (2020)
158. Teo E J et al. *Nanoscale* **6** 3243 (2014)
159. Teo E J et al. *Appl. Phys. A* **117** 719 (2014)
160. Nikolaev I V et al. *Tech. Phys. Lett.* **47** 305 (2021); *Pis'ma Zh. Tekh. Fiz.* **47** (6) 44 (2021)
161. Yin X et al., in *Proc. SPIE* **10697** 106974R (2018)
162. Li L et al. *Results Phys.* **19** 103356 (2020)
163. Toyoda N et al. *Nucl. Instrum. Meth. Phys. Res. B* **148** 639 (1999)
164. Ieshkin A E et al. *Moscow Univ. Phys. Bull.* **71** 87 (2016); *Vestn. Mosk. Univ. Fiz. Astron.* **1** 72 (2016)
165. Ieshkin A E et al. *Tech. Phys. Lett.* **43** 50 (2017); *Pis'ma Zh. Tekh. Fiz.* **43** (2) 18 (2017)
166. Mashita T, Toyoda N, Yamada I *Jpn. J. Appl. Phys.* **49** 06GH09 (2010)
167. Korobeishchikov N G, Nikolaev I V, Roenko M A *Tech. Phys. Lett.* **45** 274 (2019); *Pis'ma Zh. Tekh. Fiz.* **45** (6) 30 (2019)
168. Manenkov A A *Opt. Eng.* **53** 010901 (2014)
169. Korobeishchikov N G et al. *Surf. Interfaces* **27** 101520 (2021)
170. Toyoda N, Yamada I *Nucl. Instrum. Meth. Phys. Res. B* **273** 11 (2012)
171. Takaoka G H et al. *Nucl. Instrum. Meth. Phys. Res. B* **232** 206 (2005)
172. Aoki T, Matsuo J, Takaoka G *Nucl. Instrum. Meth. Phys. Res. B* **202** 278 (2003)
173. Nakayama Y et al. *Nucl. Instrum. Meth. Phys. Res. B* **241** 618 (2005)
174. Seki T, Aoki T, Matsuo J *AIP Conf. Proc.* **1066** 423 (2008)
175. Kyoung Y K et al. *Surf. Interface Anal.* **45** 150 (2013)
176. Shemukhin A A et al. *Nucl. Instrum. Meth. Phys. Res. B* **354** 274 (2015)
177. Isogai H et al. *Nucl. Instrum. Meth. Phys. Res. B* **257** 683 (2007)
178. Shao L et al. *Appl. Phys. Lett.* **102** 101604 (2013)
179. Zanaveskin M L et al. *Crystallogr. Rep.* **53** 701 (2008); *Kristallografiya* **53** 740 (2008)
180. Toyoda N *MRS Adv.* **1** 357 (2016)
181. Aoki T, Matsuo J *Nucl. Instrum. Meth. Phys. Res. B* **261** 639 (2007)
182. Kakuta S et al. *Nucl. Instrum. Meth. Phys. Res. B* **257** 677 (2007)
183. Chu W K et al. *Appl. Phys. Lett.* **72** 246 (1998)
184. Fathy D et al. *Mater. Lett.* **44** 248 (2000)
185. Bourelle E et al. *Nucl. Instrum. Meth. Phys. Res. B* **241** 622 (2005)
186. Suzuki A et al. *Nucl. Instrum. Meth. Phys. Res. B* **257** 649 (2007)
187. Kakekhani A, Ismail-Beigi S, Altman E I *Surf. Sci.* **650** 302 (2016)
188. Wang C et al. *Nature* **562** 101 (2018)
189. Skryleva E A et al. *Surf. Interfaces* **26** 101428 (2021)
190. Siew S Y et al. *Opt. Express* **26** 4421 (2018)
191. Zorina M V et al. *Tech. Phys. Lett.* **42** 844 (2016); *Pis'ma Zh. Tekh. Fiz.* **42** (16) 34 (2016)
192. Ieshkin A E et al. *Nucl. Instrum. Meth. Phys. Res. B* **460** 165 (2019)
193. Svyakhovskiy S E, Maydykovsky A I, Murzina T V *J. Appl. Phys.* **112** 013106 (2012)
194. Ieshkin A E, Svyakhovskiy S E, Chernysh V S *Vacuum* **148** 272 (2018)
195. Toyoda N et al. *Jpn. J. Appl. Phys.* **49** 06GH13 (2010)
196. Toyoda N et al. *J. Appl. Phys.* **105** 07C127 (2009)
197. Nagato K et al. *IEEE Trans. Magn.* **46** 2504 (2010)
198. Wu A T, Swenson D R, Insepov Z *Phys. Rev. ST Accel. Beams* **13** 093504 (2010)
199. Insepov Z et al. *AIP Conf. Proc.* **1099** 46 (2009)
200. Swenson D R, Degenkolb E, Insepov Z *Physica C* **441** 75 (2006)
201. Chernysh V S et al. *J. Instrum.* **16** T02007 (2021)
202. Pelenovich V et al. *Acta Phys. Sin.* **70** 053601 (2021)
203. Nikolaev I V et al. *Tech. Phys. Lett.* **47** 301 (2021); *Pis'ma Zh. Tekh. Fiz.* **47** (6) 44 (2021)
204. Fenner D B et al., in *Proc. SPIE* **4468** 17 (2001)
205. Nishiyama A et al. *AIP Conf. Proc.* **475** 421 (1999)
206. Bakun A D et al. *Appl. Surf. Sci.* **523** 146384 (2020)
207. Aoki T et al. *Nucl. Instrum. Meth. Phys. Res. B* **206** 861 (2003)
208. Ieshkin A E et al. *Nucl. Instrum. Meth. Phys. Res. B* **421** 27 (2018)
209. Huang, Q et al. *Nat. Commun.* **10** 2437 (2019)
210. Toyoda N, Mashita T, Yamada I *Nucl. Instrum. Meth. Phys. Res. B* **232** 212 (2005)
211. Toyoda N et al. *Appl. Phys. Rev.* **6** 020901 (2019)
212. Norris S A, Aziz M J *Appl. Phys. Rev.* **6** 011311 (2019)
213. Cuerno R, Kim J S *J. Appl. Phys.* **128** 180902 (2020)
214. Maciazek D, Kanski M, Postawa Z *Anal. Chem.* **92** 7349 (2020)
215. Sumie K, Toyoda N, Yamada I *Nucl. Instrum. Meth. Phys. Res. B* **307** 290 (2013)
216. Lozano O et al. *AIP Adv.* **3** 062107 (2013)
217. Tilakaratne B P, Chen Q Y, Chu W K *Materials* **10** 1056 (2017)
218. Zeng X et al. *Beilstein J. Nanotechnol.* **11** 383 (2020)
219. Kireev D S, Ieshkin A E, Shemukhin A A *Tech. Phys. Lett.* **46** 409 (2020); *Pis'ma Zh. Tekh. Fiz.* **46** (9) 3 (2020)
220. Ieshkin A et al. *Mater. Lett.* **272** 127829 (2020)
221. Saleem I et al. *Nucl. Instrum. Meth. Phys. Res. B* **380** 20 (2016)
222. Saleem I, Chu W K *Sens. Biosensing Res.* **11** 14 (2016)
223. Saleem I, Widger W, Chu W K *Appl. Surf. Sci.* **411** 205 (2017)
224. Radny T, Gnaser H *Nanoscale Res. Lett.* **9** 403 (2014)
225. Sanatinia R et al. *Nanotechnol.* **26** 415304 (2015)
226. Murdoch B J et al. *Appl. Phys. Lett.* **111** 081603 (2017)
227. Takagi H, Kurashima Y, Suga T *ECS Trans.* **75** (9) 3 (2016)
228. Toyoda N et al. *Jpn. J. Appl. Phys.* **57** 02BA02 (2018)
229. Ikeda S, Sasaki T, Toyoda N, in *2017 5th Intern. Workshop on Low Temperature Bonding for 3D Integration, LTB-3D, 16 – 18 May 2017* (Piscataway, NJ: IEEE, 2017) p. 66
230. Toyoda N et al. *ECS Trans.* **75** 9 (2016)
231. Shiau D K *Surf. Coatings Technol.* **365** 173 (2019)
232. Stewart C A C et al. *Appl. Surf. Sci.* **456** 701 (2018)
233. Yamada I et al. *Curr. Opin. Solid State Mater. Sci.* **19** 12 (2015)
234. https://www.exogenesis.us/biotechnology/publications
235. Khoury J et al. *Nucl. Instrum. Meth. Phys. Res. B* **307** 630 (2013)
236. Kirkpatrick S et al., in *2016 IEEE 16th Intern. Conf. on Nanotechnology, IEEE-NANO, 22 – 25 Aug. 2016* (Piscataway, NJ: IEEE, 2016) p. 710
237. Yamada I, Khoury J *MRS Proc.* **1354** 301 (2011)
238. Cleveland C L, Landman U *Science* **257** 355 (1992)
239. Insepov Z, Yamada I *Nucl. Instrum. Meth. Phys. Res. B* **112** 16 (1996)
240. Ieshkin A E et al. *Surf. Coatings Technol.* **404** 126505 (2020)
241. Toyoda N, Yamada I *Phys. Procedia* **66** 556 (2015)
242. Takaoka G H et al. *Surf. Coatings Technol.* **206** 869 (2011)
243. Ryuto H et al. *Rev. Sci. Instrum.* **85** 02C301 (2014)
244. Toyoda N et al. *Mater. Chem. Phys.* **54** 106 (1998)
245. Ogawa A, Toyoda N, Yamada I *Surf. Coatings Technol.* **306** 187 (2016)
246. Yamaguchi A et al. *Jpn. J. Appl. Phys.* **52** 05EB05 (2013)

247. Seki T et al. *Jpn. J. Appl. Phys.* **55** 06HB01 (2016)
248. Seki T et al. *Jpn. J. Appl. Phys.* **56** 06HB02 (2017)
249. Seki T et al. *Appl. Phys. Lett.* **110** 182105 (2017)
250. Toyoda N, Ogawa A *J. Phys. D* **50** 184003 (2017)
251. Toyoda N, Uematsu K *Jpn. J. Appl. Phys.* **58** SEEA01 (2019)
252. Borland J et al., in *Electrochemical Society Proceedings* Vol. 2004-07 (Eds D Harame et al.) (Pennington: The Electrochemical Society, Inc., 2004) p. 769
253. Hautala J et al. *AIP Conf. Proc.* **866** 174 (2006)
254. Maciazek D, Postawa Z *Acta Phys. Pol. A* **136** 260 (2019)
255. Benninghoven A, Rüdenauer F G, Werner H W *Secondary Ion Mass Spectrometry*: *Basic Concepts, Instrumental Aspects, Applications, and Trends* (Chemical Analysis, Vol. 86) (New York: J. Wiley, 1987)
256. Tolstoguzov A B "Perspektivnye napravleniya razvitiya metoda vtorichno-ionnoi mass-spektrometrii" ("Promising directions in the development of the secondary-ion mass spectrometry"), in *Obzory po Elektronnoi Tekhnike* (Reviews of Electronic Technology) (Ser. Technology, Production Management, and Equipment, No. 5 (1604)) (Moscow: TsNII Elektronika, 1991) p. 67
257. Cherepin V T *Ionnyi Mikrozondovyi Analiz* (Ion Microprobe Analysis) (Kiev: Naukova Dumka, 1992)
258. Tolstogouzov A B et al. *Instrum. Exp. Tech.* **58** 1 (2015); *Prib. Tekh. Eksp.* (1) 5 (2015)
259. Mahoney C M (Ed.) *Cluster Secondary Ion Mass Spectrometry*: *Principles and Applications* (Hoboken, NJ: John Wiley and Sons, 2013)
260. Ninomiya S et al. *Nucl. Instrum. Meth. Phys. Res. B* **256** 493 (2007)
261. Rzeznik L et al. *J. Phys. Chem. C* **112** 521 (2008)
262. Cristaudo V et al. *Appl. Surf. Sci.* **536** 147716 (2021)
263. Lee J L S et al. *Anal. Chem.* **82** 98 (2010)
264. Mochiji K et al. *Rapid Commun. Mass Spectrom.* **23** 648 (2009)
265. Delcorte A, Garrison B J, Hamraoui K *Surf. Interface Anal.* **43** 16 (2011)
266. Mochiji K *J. Anal. Bioanal. Tech.* **S2** 001 (2014)
267. Rabbani S et al. *Anal. Chem.* **83** 3793 (2011)
268. Benguerba M *Nucl. Instrum. Meth. Phys. Res. B* **420** 27 (2018)
269. Williams P, Mahoney C M, in *Cluster Secondary Ion Mass Spectrometry*: *Principles and Applications* (Ed. C M Mahoney) (Hoboken, NJ: John Wiley and Sons, 2013) p. 313
270. Mahoney C M et al., in *Cluster Secondary Ion Mass Spectrometry*: *Principles and Applications* (Ed. C M Mahoney) (Hoboken, NJ: John Wiley and Sons, 2013) p. 117
271. Gillen G, Bennett J, in *Cluster Secondary Ion Mass Spectrometry*: *Principles and Applications* (Ed. C M Mahoney) (Hoboken, NJ: John Wiley and Sons, 2013) p. 247
272. Rading D et al. *Surf. Interface Anal.* **45** 171 (2013)
273. Depth profile analysis of organic materials by GCIB-TOF-SIMS, https://www.toray-research.co.jp/en/technicaldata/pdf/TechData_P00905E.pdf
274. Noda et al. *J. Vac. Sci. Technol. B* **38** 034003 (2020)
275. Delcorte A, Poleunis C *J. Phys. Chem. C* **123** 19704 (2019)
276. Delmez V et al. *J. Phys. Chem. Lett.* **12** 952 (2021)
277. Mouhib T et al. *Surf. Interface Anal.* **45** 46 (2013)
278. Rabbani S S *Anal. Chem.* **87** 2367 (2015)
279. Wucher A, Tian H, Winograd N *Rapid Commun. Mass Spectrom.* **28** 396 (2014)
280. Razo I B *Rapid Commun. Mass Spectrom.* **29** 1851 (2015)
281. Tian H, Wucher A, Winograd N *J. Am. Soc. Mass Spectrom.* **27** 285 (2016)
282. Lee S J et al. *Appl. Surf. Sci.* **572** 151467 (2022)
283. Tolstogouzov A B "Combined source of mixed-composition gas cluster ion beam", Patent ZL 2018,1,1165407,4 (2018)
284. Wucher A, Fisher G L, Mahoney C M, in *Cluster Secondary Ion Mass Spectrometry*: *Principles and Applications* (Ed. C M Mahoney) (Hoboken, NJ: John Wiley and Sons, 2013) p. 207
285. Vickerman J, Winograd N, in *Cluster Secondary Ion Mass Spectrometry*: *Principles and Applications* (Ed. C M Mahoney) (Hoboken, NJ: John Wiley and Sons, 2013) p. 269
286. IONOPTIKA. J105 SIMS, https://ionoptika.com/products/j105-sims/
287. Fletcher J S et al. *Anal. Chem.* **80** 9058 (2008)
288. Hill R et al. *Surf. Interface Anal.* **43** 506 (2011)
289. Nefedov V I *Rentgenoelektronnaya Spektroskopiya Khimicheskikh Soedinenii* (X-ray Electron Spectroscopy of Chemical Compounds) (Moscow: Khimiya, 1984)
290. Friedbacher H, Bubert G (Eds) *Surface and Thin Film Analysis*: *A Compendium of Principles, Instrumentation, and Applications* (Weinheim: Wiley-VCH, 2011)
291. Stevie F A, Donley C L *J. Vac. Sci. Technol. A* **38** 063204 (2020)
292. Toray Research Center. XPS analysis using the GCIB etching, https://www.toray-research.co.jp/en/technicaldata/pdf/TechData_P01179E.pdf
293. Miisho A, Inaba M *J. Surf. Anal.* **24** 47 (2017)
294. Romanyuk O et al. *Appl. Surf. Sci.* **514** 145903 (2020)
295. Finšgar M *Corros. Sci.* **169** 108632 (2020)
296. Theodosiou A et al. *Appl. Surf. Sci.* **506** 144764 (2020)
297. SPECSGROUP. EnviroESCA, https://www.specs-group.com/nc/enviro/products/detail/enviroesca/
298. Insepov Z et al. *Phys. Rev. B* **61** 8744 (2000)
299. Kinslow R (Ed.) *High-Velocity Impact Phenomena* (New York: Academic Press, 1970)
300. Toyoda N, in *2016 IEEE 16th Intern. Conf. on Nanotechnology, IEEE-NANO, 22 – 25 Aug. 2016* (Piscataway, NJ: IEEE, 2016) p. 381
301. Onorati E et al. *Thin Solid Films* **625** 35 (2017)
302. Mochiji K et al. *Rapid Commun. Mass Spectrom.* **28** 2141 (2014)
303. Poleunis C, Cristaudo V, Delcorte A *J. Am. Soc. Mass Spectrom.* **29** 4 (2018)
304. Chundak M et al. *Appl. Surf. Sci.* **533** 147473 (2020)